Supplementary Information

Siberian and temperate ecosystems shape Northern Hemisphere atmospheric CO_2 seasonal amplification

Xin Lin[a,1], Brendan M. Rogers[b], Colm Sweeney[c], Frédéric Chevallier[d], Mikhail Arshinov[e], Edward Dlugokencky[c], Toshinobu Machida[f], Motoki Sasakawa[f], Pieter Tans[c], Gretchen Keppel-Aleks[a,1]

[a]Climate and Space Sciences and Engineering, University of Michigan, Ann Arbor, MI 48109, USA

[b]Woods Hole Research Center, Falmouth, MA 02540, USA

[c]Global Monitoring Laboratory, National Oceanic and Atmospheric Administration, Boulder, CO 80305, USA

[d]Laboratoire des Sciences du Climat et de l'Environnement/Institut Pierre Simon Laplace, Commissariat à l'Énergie Atomique et aux Énergies Alternatives–CNRS–Université de Versailles Saint-Quentin-en-Yvelines, Université Paris-Saclay, F-91191 Gif-sur-Yvette, France

[e]V.E. Zuev Institute of Atmospheric Optics, Russian Academy of Sciences, Siberian Branch, Tomsk 634055, Russia

[f]Center for Global Environmental Research, National Institute for Environmental Studies, Tsukuba, Ibaraki, 305-8506, Japan

[1]To whom correspondence may be addressed. Email: xinlinn@umich.edu or gkeppela@umich.edu

This PDF file includes:

Table S1 The geographical areas (unit: 10^6 km^2) for the 13 tagged regions and six aggregated regions, corresponding to **Fig. 1**.

Aggregated region	Tagged region	Geographical areas
NH_HighNA (15.5)	NA_Arc	12.2
	NA_Bor	3.3
NH_HighEU (4.0)	EU_Arc	2.9
	EU_Bor	1.1
NH_HighSIB (14.2)	SIB_Arc	9.2
	SIB_BorEn	2.9
	SIB_BorDn	2.0
NH_Mid (45.8)	NH_MidNat	41.6
	NH_MidCrop	4.2
NH_Trop (58.0)	NH_TropNat	55.5
	NH_TropCrop	2.5
SH (68.5)	SH_Trop	50.9
	SH_ExTrop	17.6

Table S2 Configurations of CO_2 inversion systems for CAMSv17r1 and CT2017.

		CAMSv17r1	CT2017
Available period		1979–2017	2000–2016
Resolution		1.875° × 3.75° 39 vertical layers	1° × 1° 25 vertical layers
Transport model		LMDz5A	TM5
Meteorology		ERA-Interim	ERA-Interim
Observation		Surface observations from 111 sites, Siberian tall tower measurements not included	254 sites, including aircraft and ship measurements, Siberian tall tower measurements also included
Prior fluxes	Fossil fuel	EDGAR v4.2 / CDIAC / GCP	ODIAC2016 / "Miller"
	Ocean	Ref. 1	OIF / Ref. 2
	Biomass burning	GFED4.1s / GFAS	GFED4.1s / GFED_CMS
	Terrestrial biosphere	ORCHIDEE v1.9.5.2	CASA
Assimilation technique		Variational	Ensemble
Data sources		https://apps.ecmwf.int/datasets/data/cams-ghg-inversions/	https://www.esrl.noaa.gov/gmd/ccgg/carbontracker/download.php
References		Ref. 3–4	Ref. 5

Table S3 Surface stations used in this study.

	Code	Station	LAT (°)	LON (°)	ALT (m asl)	Contributor	Time period	Latitude band	Assimilated in CAMSv17r1
1	ALT[1]	Alert, Canada	82.45	-62.52	210	EC, NOAA/GML	Flask: 1985–2017	High-latitude	Yes
2	ASC[1]	Ascension Island, UK	-7.97	-14.40	85	Met Office (UK), NOAA/GML	Flask: 1979–2017	SH	Yes
3	AZR[1]	Azores, Portugal	38.75	-27.08	22	INMG, NOAA/GML	Flask: 1979–2017	Mid-latitude	Yes
4	AZV[2]	Azovo, Russia	54.71	73.03	160	NIES/CGER, RAS	Continuous: 2007–2017	Mid-latitude	No
5	BHD	Baring Head Station, New Zealand	-41.41	-174.87	85	NIWA, NOAA/GML	Flask: 1999–2017	SH	Yes
6	BRW[1]	Utqiagvik (Barrow), USA	71.32	-156.60	11	NOAA/GML	Flask: 1971–2017	High-latitude	Yes
7	BRZ[2]	Berezorechka, Russia	56.15	84.33	248	NIES/CGER, RAS	Continuous: 2002–2017	Mid-latitude	No
8	CBA[1]	Cold Bay, USA	55.20	-162.72	25	USNWS, NOAA/GML	Flask: 1978–2017	Mid-latitude	Yes
9	CGO	Cape Grim, Tasmania, Australia	-40.68	-144.69	94	CSIRO, NOAA/GML	Flask: 1984–2017	SH	Yes
10	CRZ	Crozet Island, France	-46.43	-51.85	197	LSCE, NOAA/GML	Flask: 1991–2017	SH	Yes
11	DEM[2]	Demyanskoe, Russia	59.79	70.87	126	NIES/CGER, RAS	Continuous: 2005–2017	Mid-latitude	No
12	EIC	Easter Island, Chile	-27.16	-109.43	47	DMC, NOAA/GML	Flask: 1994–2017	SH	Yes
13	GMI[1]	Mariana Island, Guam	13.39	144.66	5	Univ. of Guam, NOAA/GML	Flask: 1978–2017	Low-latitude	Yes
14	HBA	Halley Station, Antarctica, UK	-75.61	-26.21	30	BAC, NOAA/GML	Flask: 1983–2017	SH	Yes
15	IGR[2]	Igrim, Russia	63.19	64.41	56	NIES/CGER, RAS	Continuous: 2004–2013	High-latitude	No
16	IZO[1]	Izaña, Tenerife, Spain	28.31	-16.50	2378	AEMET, NOAA/GML	Flask: 1991–2017	Low-latitude	Yes
17	KRS[2]	Karasevoe, Russia	58.25	82.42	143	NIES/CGER, RAS	Continuous: 2004–2017	Mid-latitude	No
18	KUM[1]	Cape Kumukahi, USA	19.52	-154.82	3	NOAA/GML	Flask: 1971–2017	Low-latitude	Yes
19	MBC[1]	Mould Bay, Canada	76.25	-119.35	32	EC, NOAA/GML	Flask: 1980–1997	High-latitude	Yes
20	MHD[1]	Mace Head, Ireland	53.33	-9.90	8	NOAA/GML	Flask: 1991–2017	Mid-latitude	Yes
21	MID[1]	Midway, USA	28.22	-177.37	4	USFWS, NOAA/GML	Flask: 1985–2017	Low-latitude	Yes
22	MLO[1]	Mauna Loa, USA	19.54	-155.58	3399	NOAA/GML	Flask: 1969–2017	Low-latitude	Yes
23	NMB[1]	Gobabeb, Namibia	-23.58	-15.03	456	GTRC, NOAA/GML	Flask: 1997–2017	SH	Yes
24	NOY[2]	Noyabrsk, Russia	63.43	75.78	151	NIES/CGER, RAS	Continuous: 2005–2017	High-latitude	No
25	NWR[1]	Niwot Ridge, USA	40.05	-105.59	3523	INSTAAR, NOAA/GML	Flask: 1967–2017	Mid-latitude	Yes
26	PSA[1]	Palmer Station, Antarctica, USA	-64.92	-64.00	10	NSF, NOAA/GML	Flask: 1978–2017	SH	Yes
27	SEY[1]	Mahe Island, Seychelles	-4.68	55.53	2	SBS, NOAA/GML	Flask: 1980–2017	SH	Yes
28	SHM[1]	Shemya Island, USA	52.75	174.10	26	Chugach, NOAA/GML	Flask: 1985–2017	Mid-latitude	Yes

29	SMO[1]	Tutuila, American Samoa	-15.25	-170.56	42	NOAA/GML	Flask: 1972–2017	SH	Yes
30	SPO[1]	South Pole, Antarctica, USA	-89.98	-24.80	2810	NSF, NOAA/GML	Flask: 1975–2017	SH	Yes
31	STM[1]	Ocean Station M, Norway	66.00	2.00	7	NMI, NOAA/GML	Flask: 1981–2009	High-latitude	Yes
32	SUM[1]	Summit, Denmark	72.58	-38.48	3215	NSF, NOAA/GML	Flask: 1997–2017	High-latitude	Yes
33	SYO[1]	Syowa Station, Antarctica, Japan	-69.01	39.59	14	NIPR, NOAA/GML	Flask: 1986–2017	SH	Yes
34	SVV[2]	Savvushka, Russia	51.33	82.13	547	NIES/CGER, RAS	Continuous: 2006–2014	Mid-latitude	No
35	TER[3]	Teriberka, Russia	69.20	35.10	40	MGO	Flask: 1988–2017	High-latitude	No
36	TIK[1]	Tiksi, Russia	71.60	128.89	29	MGO, NOAA/GML	Flask: 2011–2017	High-latitude	No
37	USH[1]	Ushuaia, Argentina	-54.85	-68.31	12	SMN, NOAA/GML	Flask: 1994–2017	SH	Yes
38	VGN[2]	Vaganovo, Russia	54.50	62.32	277	NIES/CGER, RAS	Continuous: 2008–2017	Mid-latitude	No
39	YAK[2]	Yakutsk, Russia	62.09	129.36	341	NIES/CGER, RAS	Continuous: 2005–2013	High-latitude	No
40	ZEP[1]	Zeppelin station, Norway and Sweden	78.91	11.89	479	MISU, NOAA/GML	Flask: 1994–2017	High-latitude	Yes

[1] See Ref. 6, retrieved from ftp://aftp.cmdl.noaa.gov/data/trace_gases/co2/flask/surface/

[2] See Ref. 7–8, retrieved from http://db.cger.nies.go.jp/portal/geds/atmosphericAndOceanicMonitoring/

[3] Retrieved from https://gaw.kishou.go.jp/

Abbreviations:

AEMET – Agencia Estatal de Meteorología, Spain; BAC – British Antarctic Survey; CSIRO – Commonwealth Scientific and Industrial Research Organisation, Australia; DMC – Dirección Meteorológica de Chile; EC – Environment Canada, Canada; GTRC – Gobabeb Training and Research Center; INAMET – Instituto Nacional de Meteorologia e Geofísica, Portugal; INSTAAR – Institute of Arctic and Alpine Research, University of Colorado, USA; LSCE – Le Laboratoire des Sciences du Climat et l'Environnement; MISU – Meteorological Institute, University of Stockholm, Sweden; MGO – Voeikov Main Geophysical Observatory, Russia; NIES/CGER – National Institute for Environmental Studies/Center for Global Environmental Research, Japan; NMI – Norway Meteorological Institute, Norway; NSF – National Science Foundation, USA; NOAA/GML – National Oceanic and Atmospheric Administration/Global Monitoring Laboratory; RAS – Russian Academy of Science; SBS – Seychelles Bureau of Standards; SMN – Servicio Meteorológico Nacional, Argentina; USFWS – U. S. Fish and Wildlife Service; USNWS – U. S. National Weather Service

Table S4 Aircraft sampling networks and campaigns used in this study.

	Network/ Campaign	Sampling domain	Flask/ in-situ	Sampling frequency	Sampling altitude	Time period	Scale	Contributor	References
1	NOAA's GGGRN[1]	North America, Pacific	Flask	Vary	0–14870 m asl	1992–2016	WMO X2007	NOAA/GML	Ref. 9
2	CONTRAIL[2]	Over airports and along flights	In-situ	10s	0–13107 m asl	2005–2015	NIES09	NIES, MRI	Ref. 10–11
3	NIES/CGER[3]	Berezorechka in west Siberia	In-situ	2s	100–3113 m agl	2001–2012	NIES09	NIES/CGER, RAS	Ref. 7

[1] Retrieved from: https://www.esrl.noaa.gov/gmd/ccgg/obspack/data.php
[2] Retrieved from: http://www.cger.nies.go.jp/contrail/
[3] Retrieved from: http://db.cger.nies.go.jp/portal/geds/atmosphericAndOceanicMonitoring

Abbreviations:
CONTRAIL – Comprehensive Observation Network for TRace gases by AIrLiner; MRI – Meteorological Research Institute, Japan; NIES/CGER – National Institute for Environmental Studies/Center for Global Environmental Research, Japan; NOAA/GML – National Oceanic and Atmospheric Administration/Global Monitoring Laboratory; NOAA's GGGRN – National Oceanic and Atmospheric Administration's Global Greenhouse Gas Reference Network; RAS – Russian Academy of Science

Table S5 Mean bias and RMSE of simulated CO_2 seasonal cycle amplitudes (SCA) and trends compared to ground observations in the NH for different station groups.

	Mean SCA (ppm)		SCA trend (ppm·10yr^{-1})	
	Mean bias	RMSE	Mean bias	RMSE
Assimilated sites (NOAA's GGGRN sites)	0.1±1.4	1.3	0.15±0.31	0.34
Non-assimilated sites (Russian sites)	1.5±3.5	3.7	0.43	0.43
High-latitude assimilated sites (60°–90°N)	0.8±1.7	1.7	0.12±0.23	0.25
Mid-latitude assimilated sites (30°–60°N)	-0.1±1.4	1.3	0.42±0.27	0.48
Low-latitude assimilated sites (0°–30°N)	-0.6±0.5	0.7	-0.07±0.27	0.25

Table S6 Regional contribution to CO_2 seasonal cycle amplitudes (SCA) for stations in the northern high-, mid-, and low-latitudes, based on simulated CO_2 and tracer concentrations from CAMSv17r1 during 1980–2017. For each latitude band, the regional contribution to SCA (in ppm) was averaged across stations, corresponding to **Fig. 3*A***. The contribution in percentage (%) averaged across all stations in each latitude band is given as well in parentheses. Note that the contribution in percentage does not add up to 100%.

1980–2017	Mean SCA	HighNA	HighEU	HighSIB	NH_Mid	NH_Trop	SH
High-latitude sites (60°–90°N; n=7)	16.4±2.5	3.7±0.9 (22.5±4.1%)	1.5±1.1 (8.5±5.5%)	3.9±1.2 (23.5±5.3%)	7.5±0.8 (46.1±6.1%)	-1.0±0.1 (-6.4±0.7%)	0.4±0.0 (2.5±0.7%)
Mid-latitude sites (30°–60°N; n=5)	13.0±4.1	2.5±1.1 (18.9±5.9%)	0.6±0.2 (4.3±0.5%)	3.4±2.3 (24.4±11.3%)	6.1±1.7 (48.7±7.7%)	-0.6±0.6 (-3.5±5.5%)	0.4±0.0 (3.4±1.0%)
Low-latitude sites (0°–30°N; n=5)	7.1±1.2	0.9±0.3 (12.9±1.7%)	0.3±0.1 (4.0±0.8%)	1.4±0.6 (18.7±5.5%)	3.4±0.8 (47.1±3.7%)	0.8±0.7 (12.7±12.1%)	0.2±0.2 (2.2±2.5%)

Table S7 Regional contribution to CO_2 seasonal cycle amplitudes (SCA) for stations in the northern high-, mid-, and low-latitudes, based on simulated CO_2 and tracer concentrations from **(a)** CAMSv17r1 and **(b)** CT2017 during 2000–2016. For each latitude band, the regional contribution to SCA (in ppm) is averaged across stations. The contribution in percentage (%) averaged across all stations in each latitude band is given as well in parentheses. Note that the contribution in percentage does not add up to 100%.

(a)

2000–2016	Mean SCA	HighNA	HighEU	HighSIB	NH_Mid	NH_Trop	SH
High-latitude sites (60°–90°N; n=7)	17.5±2.6	3.8±1.0 (22.0±4.1%)	1.4±1.1 (7.6±5.0%)	4.4±1.2 (24.7±5.2%)	7.9±0.9 (45.5±6.5%)	-0.9±0.1 (-5.5±0.6%)	0.4±0.0 (2.4±0.7%)
Mid-latitude sites (30°–60°N; n=5)	13.6±4.4	2.6±1.2 (18.3±5.3%)	0.6±0.2 (4.1±0.4%)	3.7±2.3 (25.3±10.4%)	6.4±1.8 (48.2±7.6%)	-0.6±0.5 (-3.4±4.3%)	0.4±0.0 (3.5±1.1%)
Low-latitude sites (0°–30°N; n=5)	7.2±1.4	0.9±0.3 (12.7±1.7%)	0.3±0.1 (3.9±0.8%)	1.4±0.6 (18.7±5.0%)	3.6±0.9 (48.9±3.5%)	0.7±0.7 (11.0±11.2%)	0.2±0.2 (2.4±2.6%)

(b)

2000–2016	Mean SCA	HighNA	HighEU	HighSIB	NH_Mid	NH_Trop	SH
High-latitude sites (60°–90°N; n=7)	17.5±2.2	2.8±0.5 (15.9±2.1%)	1.3±1.0 (7.1±4.6%)	5.1±1.1 (29.3±5.3%)	8.0±0.8 (46.1±4.5%)	-0.3±0.0 (-1.7±0.2%)	0.1±0.0 (0.8±0.4%)
Mid-latitude sites (30°–60°N; n=5)	14.1±4.4	1.9±0.8 (13.4±4.0%)	0.6±0.2 (3.9±0.4%)	4.4±2.4 (29.6±8.6%)	6.8±1.5 (50.1±7.2%)	-0.2±0.1 (-1.2±1.1%)	0.2±0.1 (1.8±1.3%)
Low-latitude sites (0°–30°N; n=5)	7.5±1.8	0.8±0.2 (10.1±0.6%)	0.3±0.1 (3.6±0.4%)	1.7±0.7 (22.2±3.4%)	4.2±1.1 (56.5±1.0%)	0.2±0.2 (3.1±3.9%)	0.2±0.1 (2.9±0.6%)

Table S8 Contribution of different regions to changes in CO_2 seasonal cycle amplitudes (ΔSCA) for stations in northern high-, mid-, and low-latitudes, based on simulated CO_2 and tracer concentrations from CAMSv17r1 during 1980–2017. For each latitude band, the regional contribution to ΔSCA (in ppm) is averaged across stations, corresponding to **Fig. 3*C***. The contribution in percentage (%) averaged across all stations in each latitude band is given as well in parentheses. Note that the contribution in percentage does not add up to 100%.

1980–2017	ΔSCA	HighNA	HighEU	HighSIB	NH_Mid	NH_Trop	SH
High-latitude sites (60°–90°N; n=7)	3.8±0.4	0.5±0.4 (11.4±8.9%)	-0.1±0.1 (-2.2±2.3%)	1.6±0.3 (42.2±3.7%)	1.5±0.3 (38.8±9.8%)	0.3±0.1 (7.0±2.1%)	0.0±0.0 (0.9±1.0%)
Mid-latitude sites (30°–60°N; n=5)	2.4±1.3	0.1±0.2 (7.9±12.9%)	0.0±0.1 (1.7±4.2%)	1.1±0.5 (61.4±36.5%)	0.9±0.6 (31.8±21.9%)	0.1±0.2 (-11.4±37.7%)	0.1±0.0 (8.9±12.7%)
Low-latitude sites (0°–30°N; n=5)	0.6±0.6	0.0±0.1 (1.5±32.1%)	0.0±0.1 (1.2±%)	0.1±0.2 (33.4±37.7%)	0.6±0.2 (70.6±238.2%)	-0.2±0.2 (-15.3±240.1%)	0.1±0.0 (13.6±26.9%)

Table S9 Zonal analyses of the dominant contributor to changes in CO_2 seasonal cycle amplitudes (ΔSCA) for northern high-, mid-, and low-latitudes at **(a)** the surface, **(b)** 700 mb and **(c)** 500 mb. For each latitude band, the total area of pixels (S_pixel, in unit 10^6 km^2) with significant trends in SCA ($p < 0.05$) is given, as well as the area of pixels (and the area percentage) where a specific tagged region is identified as the dominant contributor.

(a) Surface

1980–2017	S_pixel	HighNA	HighEU	HighSIB	NH_Mid	Others
High-latitude pixels (60°–90°N)	36.02	1.84 (5.1%)	0 (0%)	23.03 (63.9%)	11.12 (30.9%)	0.03 (0.1%)
Mid-latitude pixels (30°–60°N)	68.82	0.46 (0.7%)	0 (0%)	19.46 (28.3%)	47.62 (69.2%)	1.28 (1.9%)
Low-latitude pixels (0°–30°N)	63.90	0 (0%)	0 (0%)	4.17 (6.5%)	26.84 (42.0%)	32.90 (51.5%)

(b) 700 mb

1980–2017	S_pixel	HighNA	HighEU	HighSIB	NH_Mid	Others
High-latitude pixels (60°–90°N)	36.43	0.42 (1.2%)	0 (0%)	7.58 (20.8%)	28.18 (77.3%)	0.25 (0.7%)
Mid-latitude pixels (30°–60°N)	79.73	0.08 (0.1%)	0 (0%)	8.05 (10.1%)	71.19 (89.3%)	0.41 (0.5%)
Low-latitude pixels (0°–30°N)	45.41	0 (0%)	0 (0%)	5.61 (12.4%)	8.34 (18.4%)	31.47 (69.3%)

(c) 500 mb

1980–2017	S_pixel	HighNA	HighEU	HighSIB	NH_Mid	Others
High-latitude pixels (60°–90°N)	36.47	0 (0%)	0 (0%)	0 (0%)	36.47 (100%)	0 (0%)
Mid-latitude pixels (30°–60°N)	77.05	0 (0%)	0 (0%)	0.45 (0.6%)	75.71 (98.3%)	0.88 (1.1%)
Low-latitude pixels (0°–30°N)	21.86	0 (0%)	0 (0%)	0.12 (0.5%)	6.87 (31.5%)	14.86 (68.0%)

Table S10 Zonal analyses of the regional contributions to changes in CO_2 seasonal cycle amplitudes (ΔSCA) for northern high-, mid-, and low-latitudes at **(a)** the surface, **(b)** 700 mb and **(c)** 500 mb. For each latitude band, the regional contribution to ΔSCA (in ppm) is averaged across pixels with positive and significant trends (i.e., ΔSCA > 0; $p < 0.05$). The contribution in percentage (%) averaged across all pixels in each latitude band is given as well in parentheses. Note that the contribution in percentage does not add up to 100%.

(a) Surface

1980–2017	ΔSCA	HighNA	HighEU	HighSIB	NH_Mid	Others
High-latitude pixels (60°–90°N)	4.1±0.9	0.5±0.6 (10.6±13.5%)	-0.1±0.2 (-3.3±5.5%)	2.1±1.0 (50.8±14.0%)	1.1±0.5 (29.6±15.9%)	0.5±0.2 (12.3±4.8%)
Mid-latitude pixels (30°–60°N)	3.4±2.2	0.2±0.6 (1.7±18.5%)	0.1±0.2 (1.4±4.9%)	1.2±0.7 (36.3±18.5%)	1.6±1.5 (47.8±32.5%)	0.5±0.5 (12.7±17.7%)
Low-latitude pixels (0°–30°N)	1.3±0.7	0.0±0.1 (-0.6±7.9%)	0.0±0.0 (0.3±2.6%)	0.4±0.2 (30.8±13.3%)	0.8±0.5 (68.8±45.0%)	0.2±0.7 (0.7±49.2%)

(b) 700 mb

1980–2017	ΔSCA	HighNA	HighEU	HighSIB	NH_Mid	Others
High-latitude pixels (60°–90°N)	3.5±0.4	0.2±0.2 (6.7±5.8%)	0.0±0.0 (-0.4±1.3%)	1.3±0.3 (37.8±7.3%)	1.6±0.3 (45.4±8.5%)	0.4±0.2 (10.5±5.9%)
Mid-latitude pixels (30°–60°N)	2.3±1.2	0.1±0.2 (3.9±8.1%)	0.0±0.1 (1.1±2.8%)	0.7±0.4 (30.2±11.3%)	1.3±0.7 (66.7±31.1%)	0.1±0.4 (-1.9±27.1%)
Low-latitude pixels (0°–30°N)	1.2±0.3	0.1±0.1 (6.8±9.0%)	0.0±0.0 (1.9±4.5%)	0.5±0.2 (46.3±16.4%)	0.6±0.5 (60.9±52.2%)	-0.1±0.7 (-15.9±67.2%)

(c) 500 mb

1980–2017	ΔSCA	HighNA	HighEU	HighSIB	NH_Mid	Others
High-latitude pixels (60°–90°N)	2.9±0.4	0.1±0.1 (4.0±3.1%)	0.0±0.0 (0.6±0.9%)	1.0±0.2 (33.9±4.5%)	1.5±0.2 (51.6±5.3%)	0.3±0.1 (9.9±4.6%)
Mid-latitude pixels (30°–60°N)	1.6±0.8	0.1±0.1 (1.3±7.4%)	0.0±0.0 (0.4±1.4%)	0.5±0.2 (32.0±10.9%)	1.2±0.4 (88.6±34.4%)	-0.2±0.3 (-22.2±36.4%)
Low-latitude pixels (0°–30°N)	0.7±0.1	0.0±0.0 (5.4±4.2%)	0.0±0.0 (1.2±1.2%)	0.4±0.1 (53.2±10.1%)	0.6±0.1 (96.1±21.2%)	-0.3±0.1 (-55.9±28.4%)

Table S11 The annual mean fluxes and flux trends over the period 1980–2017 for the six major tagged regions (** $p < 0.01$, * $p < 0.05$). For each tagged region, both integrated and per area annual mean fluxes or flux trends are given. Analyses are based on land fluxes from CAMSv17r1.

	Annual mean fluxes		Flux trends	
	Integrated ($PgC \cdot yr^{-1}$)	Per area ($gC \cdot m^{-2} \cdot yr^{-1}$)	Integrated (10^{-3} $PgC \cdot yr^{-2}$)	Per area ($gC \cdot m^{-2} \cdot yr^{-2}$)
NH_HighNA	-0.32 ± 0.13	-20.82 ± 8.26	-3.11 ± 1.85	-0.20 ± 0.12
NH_HighEU	-0.09 ± 0.05	-21.96 ± 12.99	-1.70 ± 0.73*	-0.42 ± 0.18*
NH_HighSIB	-0.17 ± 0.28	-12.34 ± 20.09	-18.82 ± 2.89**	-1.33 ± 0.20**
NH_Mid	-1.84 ± 0.37	-40.11 ± 8.10	-11.85 ± 5.21*	-0.26 ± 0.11*
NH_Trop	0.46 ± 0.60	8.00 ± 10.42	8.24 ± 8.95	0.14 ± 0.15
SH	0.03 ± 0.76	0.50 ± 11.03	-36.45 ± 9.57*	-0.53 ± 0.14*

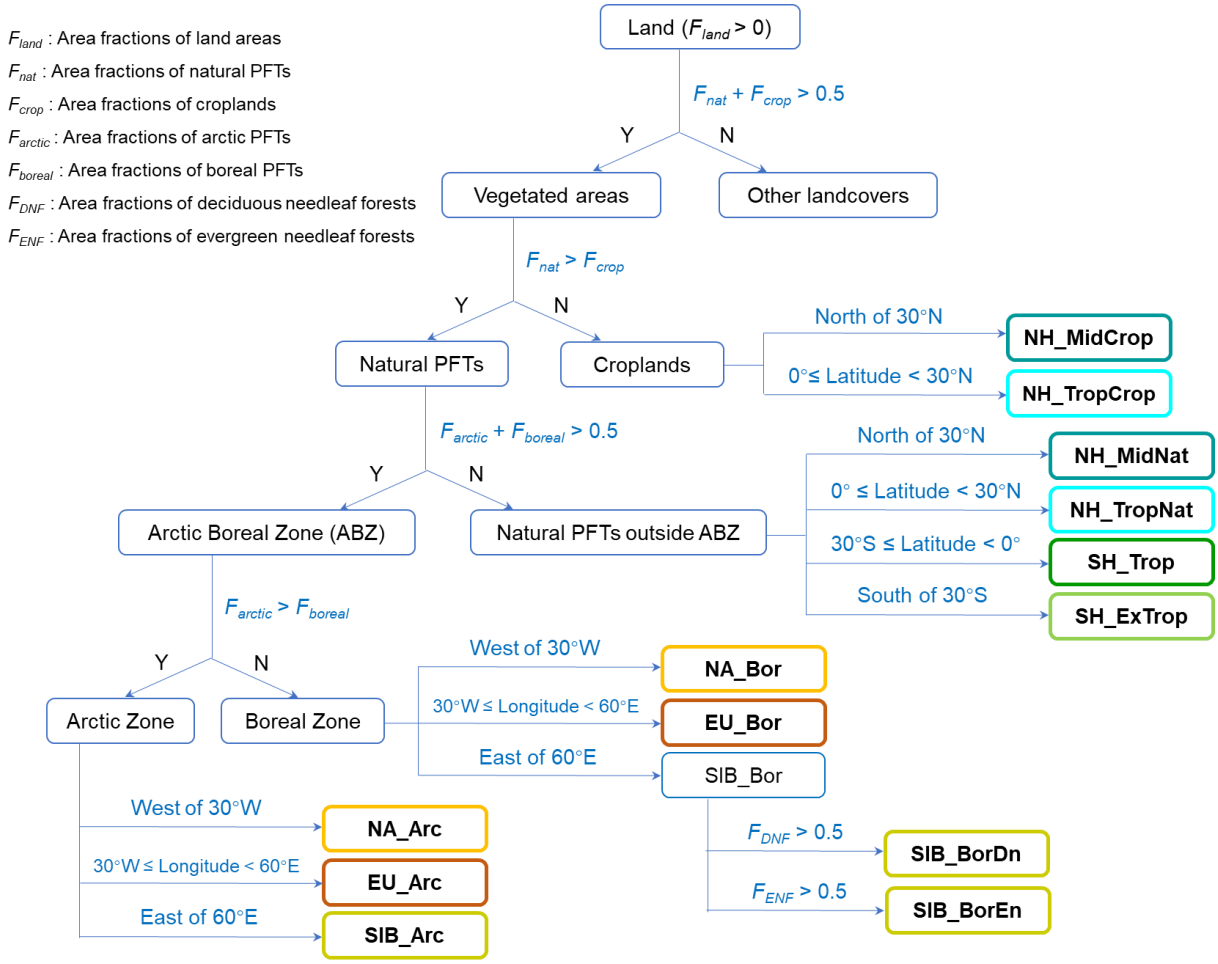

Figure S1 Flow chart showing definition of the 13 tagged regions for terrestrial ecosystems. The delineation of these regions was based on climate, continent and plant functional types (PFTs) from the Community Land Model version 5 (CLM5) for 2000. Of the 16 PFTs defined in CLM5 (see details in http://www.cesm.ucar.edu/models/clm/surface.heterogeneity.html), arctic PFTs include Arctic C3 grass and Broadleaf deciduous boreal shrubs, whereas boreal PFTs include Needleleaf evergreen boreal trees, Needleleaf deciduous boreal trees and Broadleaf deciduous boreal trees.

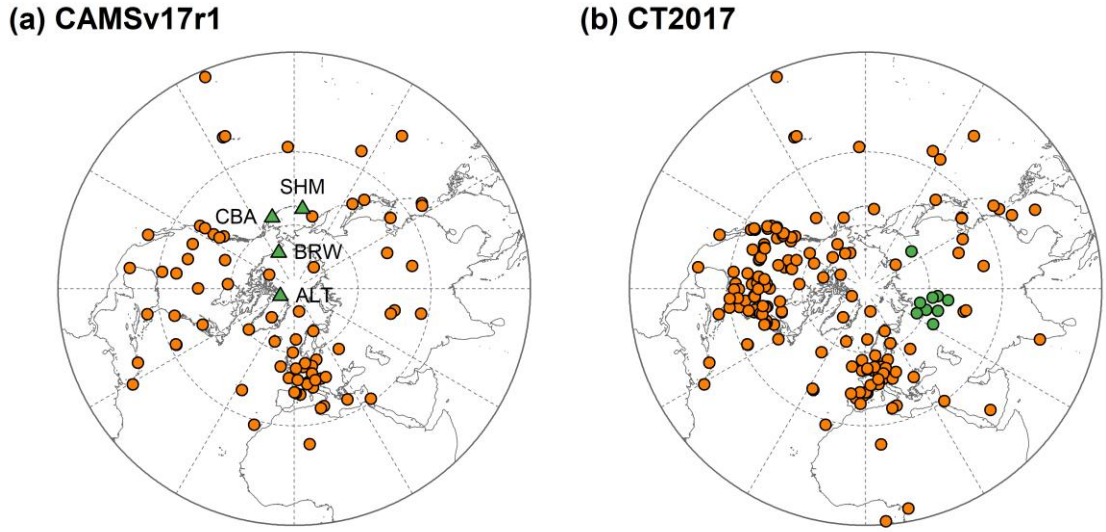

Figure S2 Locations of assimilated surface stations in the Northern Hemisphere in the CO_2 inversions: **(a)** CAMSv17r1 and **(b)** CT2017. The green triangles in **(a)** represent the four marine boundary layer stations downwind of Siberia with data record dating back to the 1980s or earlier, i.e., Alert (ALT), Utqiagvik (Barrow, BRW), Cold Bay (CBA) and Shemya Island (SHM). The green circles in **(b)** indicate the inland tall towers in Siberia, which are assimilated in CT2017 but not in CAMSv17r1.

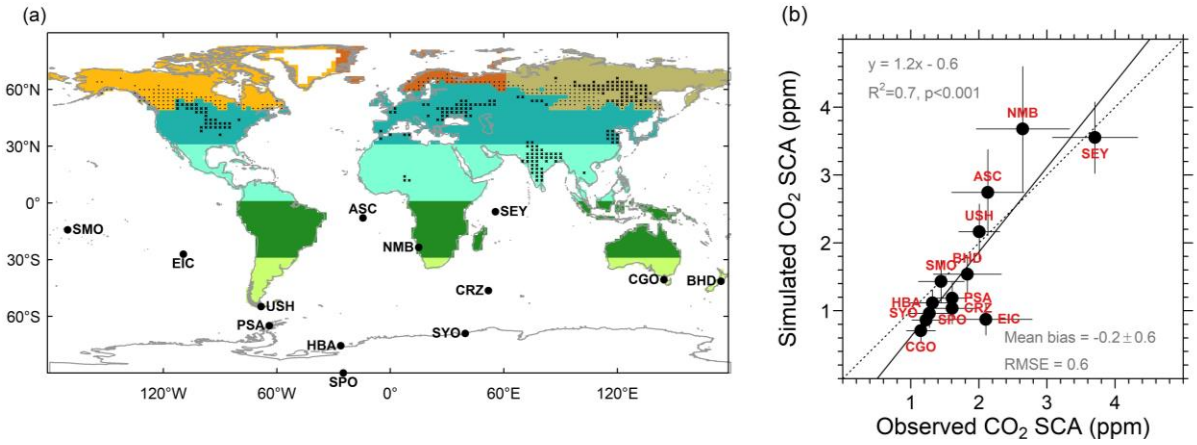

Figure S3 (a) Map of 13 surface stations in the Southern Hemisphere from the NOAA's GGGRN used for evaluation. Only stations with records longer than 15 years were selected. **(b)** Comparison of simulated versus observed CO_2 SCA at these stations. The dotted and solid lines represent the unit line and least squares regression line, respectively. Error bars denote ±1σ standard deviation.

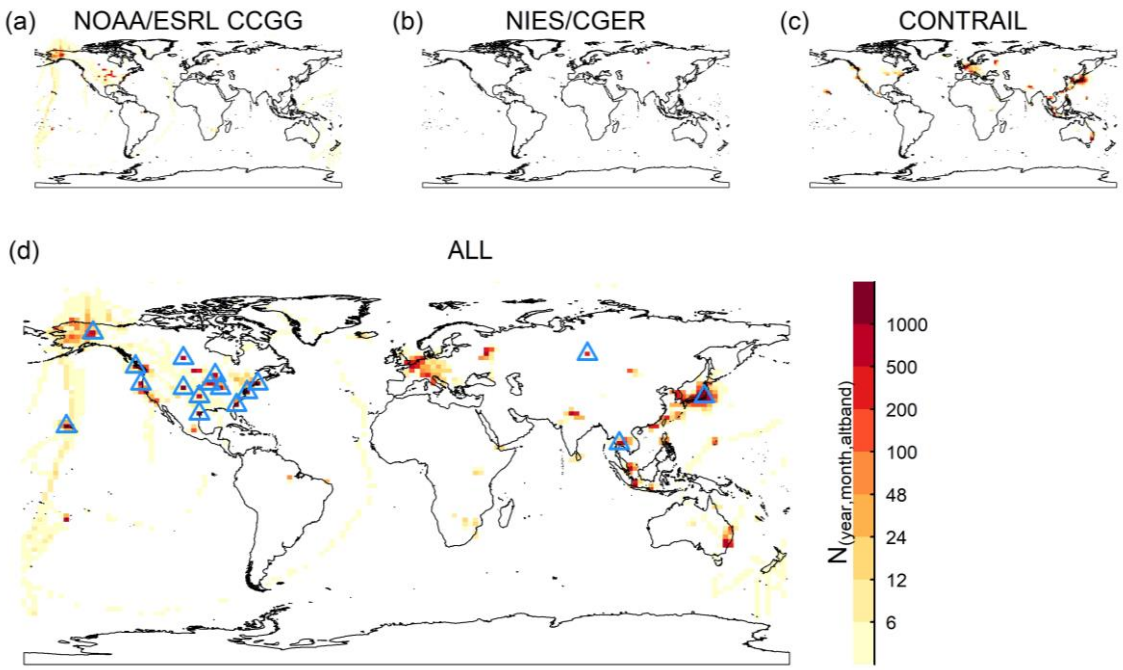

Figure S4 Spatial distribution of aircraft CO_2 vertical profiles from different networks: **(a)** NOAA's GGGRN, **(b)** NIES/CGER, and **(c)** CONTRAIL. Observations from the three networks were combined and grouped based on GEOS-Chem 2° × 2.5° model grids and 1 km altitude bins between 0 and 8 km **(d)**. Grid cells are colored by observation density, $N_{(year, month, altband)}$, which is defined as the number of different combinations of the year, month and altitude bin that an observation is sampled. We identify 17 grid cells with satisfactory record length (≥ 10 yrs) and vertical profiles for model evaluation (noted as blue triangles; also see **Fig. 1*A*** and ***SI Appendix*** **Fig. S5**).

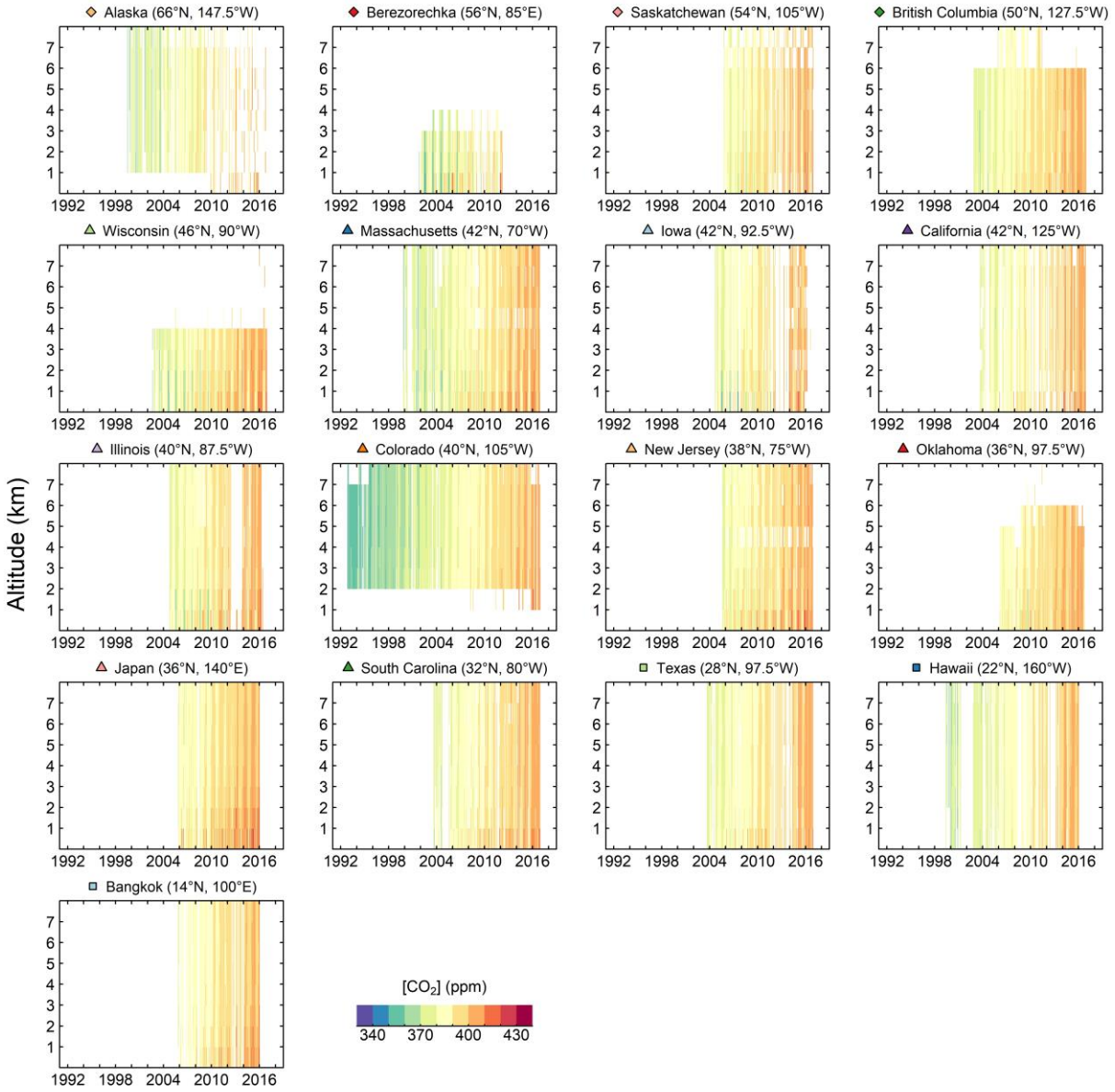

Figure S5 Time series of CO_2 concentrations between 0 km and 8 km from aircraft profiles at 17 selected grid cells for model evaluation. Each line represents an individual observation from a particular aircraft campaign within the pixel, colored by levels of CO_2 concentrations. Panels are arranged by latitudes and correspond to aircraft sites noted in **Fig. 1*A*** and ***SI Appendix* Fig. S4d**.

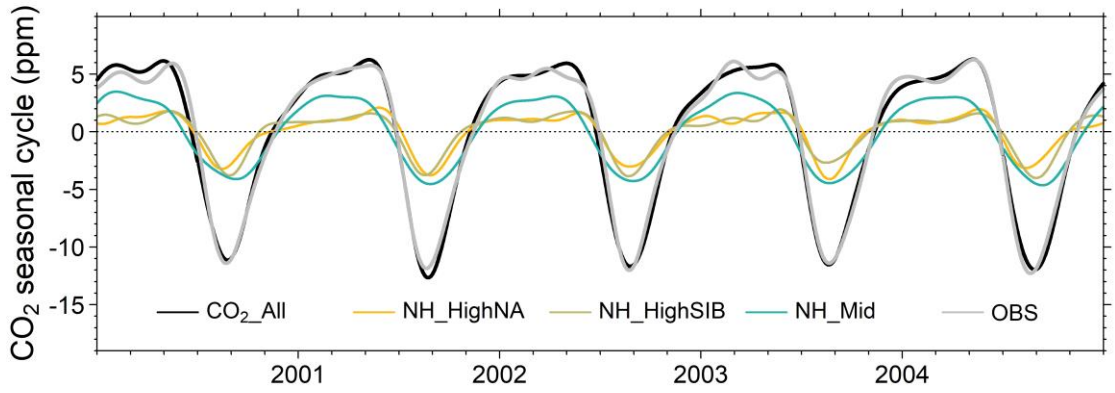

Figure S6 Simulated annual cycles of CO_2 (in black) and tracers (in colors) from different tagged regions at Utqiagvik (Barrow), Alaska, after removing long-term growth rates. The grey line indicates the observed CO_2 annual cycles after detrending. Note that for a specific year, the Julian days when the CO_2 and tracer curves reach the seasonal maxima or minima are not necessarily the same (phase shift).

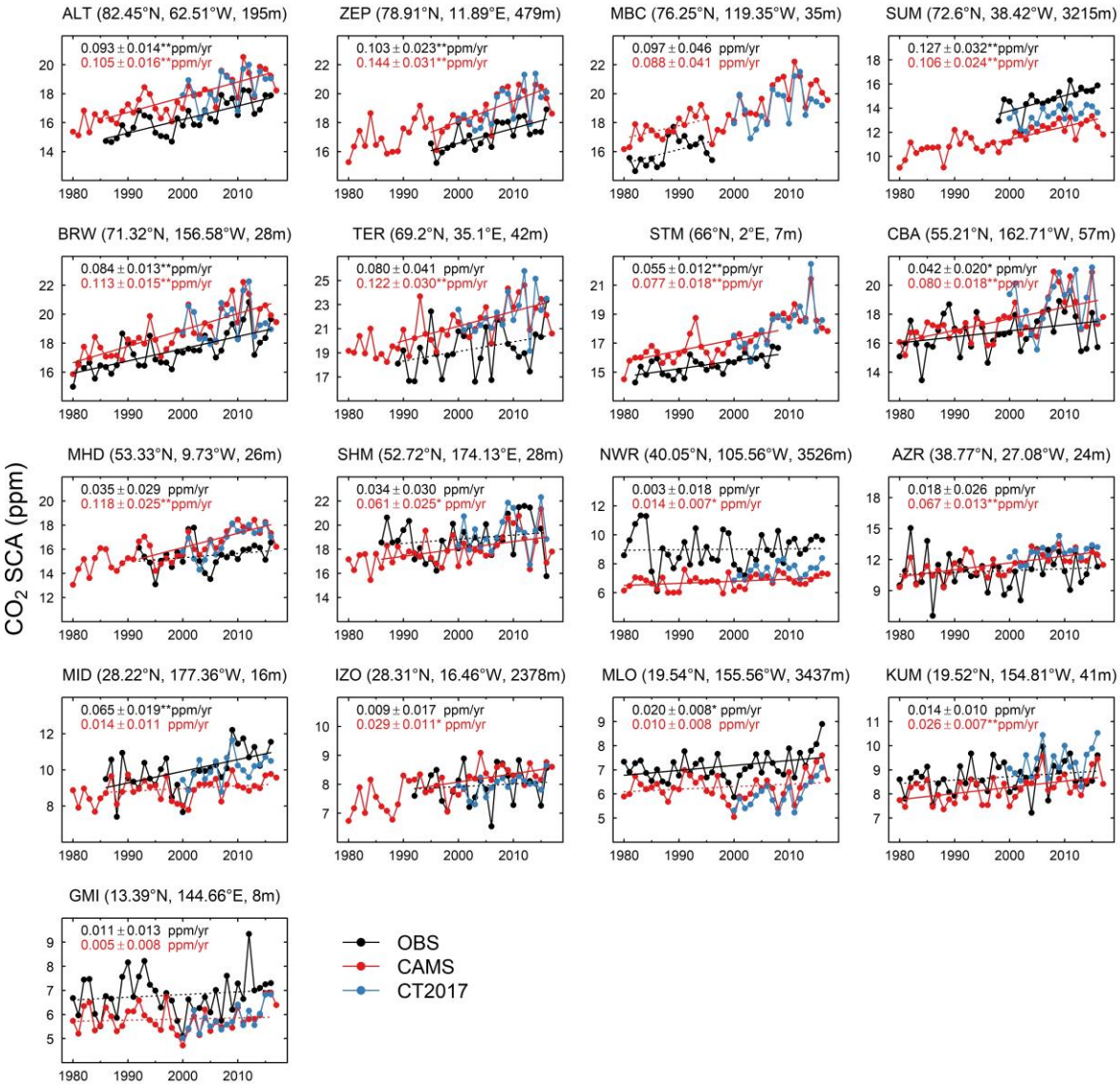

Figure S7 Time series of observed and simulated CO_2 SCA at selected stations in the Northern Hemisphere from NOAA's GGGRN and at the Russian station Teriberka (TER). For each panel, black dots indicate CO_2 SCA from observations, while red and blue dots indicate simulated SCA from CO_2 inversion products CAMSv17r1 and CT2017, respectively. Both observed and simulated CO_2 SCA from CAMSv17r1 were fitted over the time period when observations are available, with trends given as well (** $p < 0.01$, * $p < 0.05$). Solid and dotted lines indicate significant and non-significant trends, respectively. Panels are arranged by latitudes.

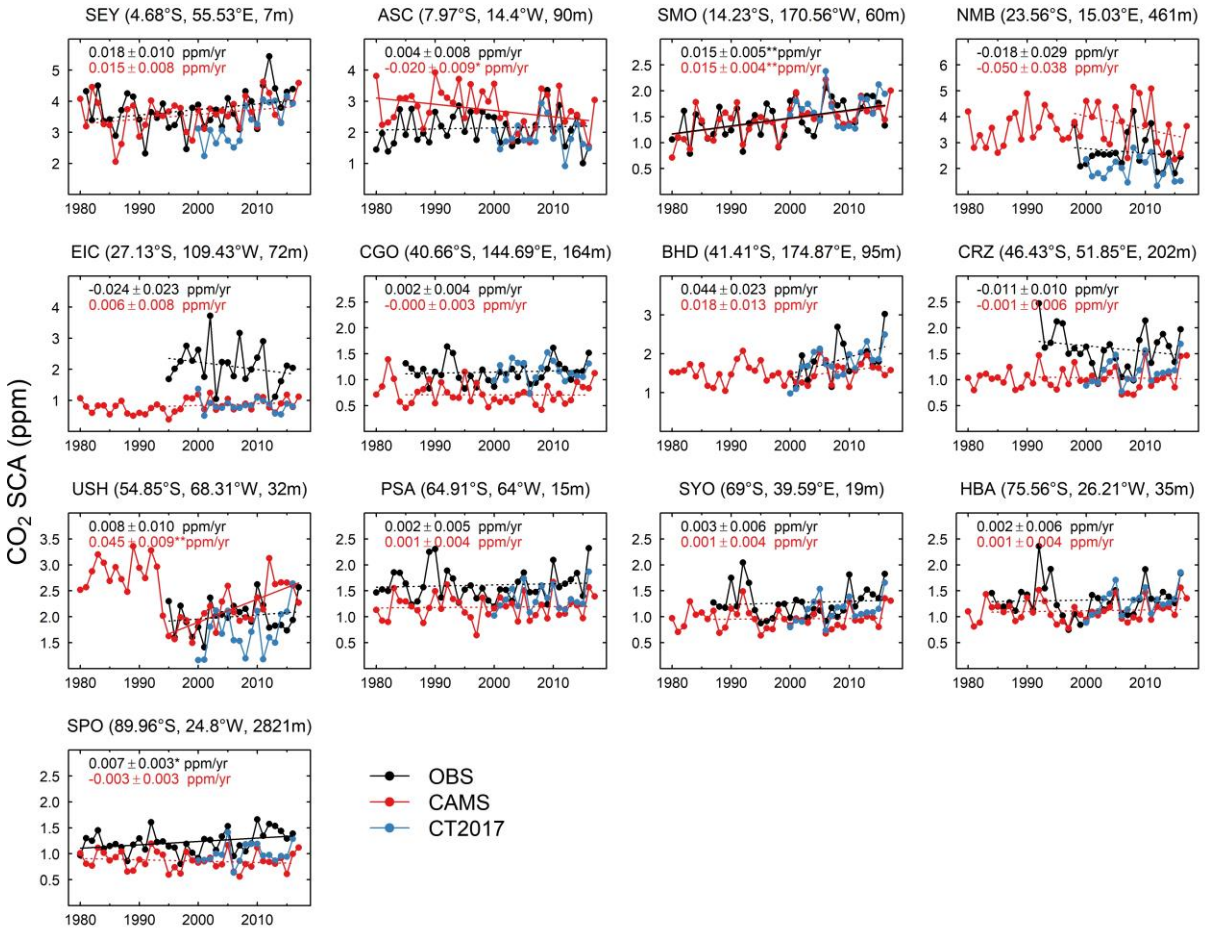

Figure S8 Time series of observed and simulated CO_2 SCA at 13 selected stations in the Southern Hemisphere from NOAA's GGGRN. For each panel, black dots indicate CO_2 SCA from observations, while red and blue dots indicate simulated SCA from CO_2 inversion products CAMSv17r1 and CT2017, respectively. Both observed and simulated CO_2 SCA from CAMSv17r1 were fitted over the time period when observations are available, with trends given as well (** $p < 0.01$, * $p < 0.05$). Solid and dotted lines indicate significant and non-significant trends, respectively. Panels are arranged by latitudes.

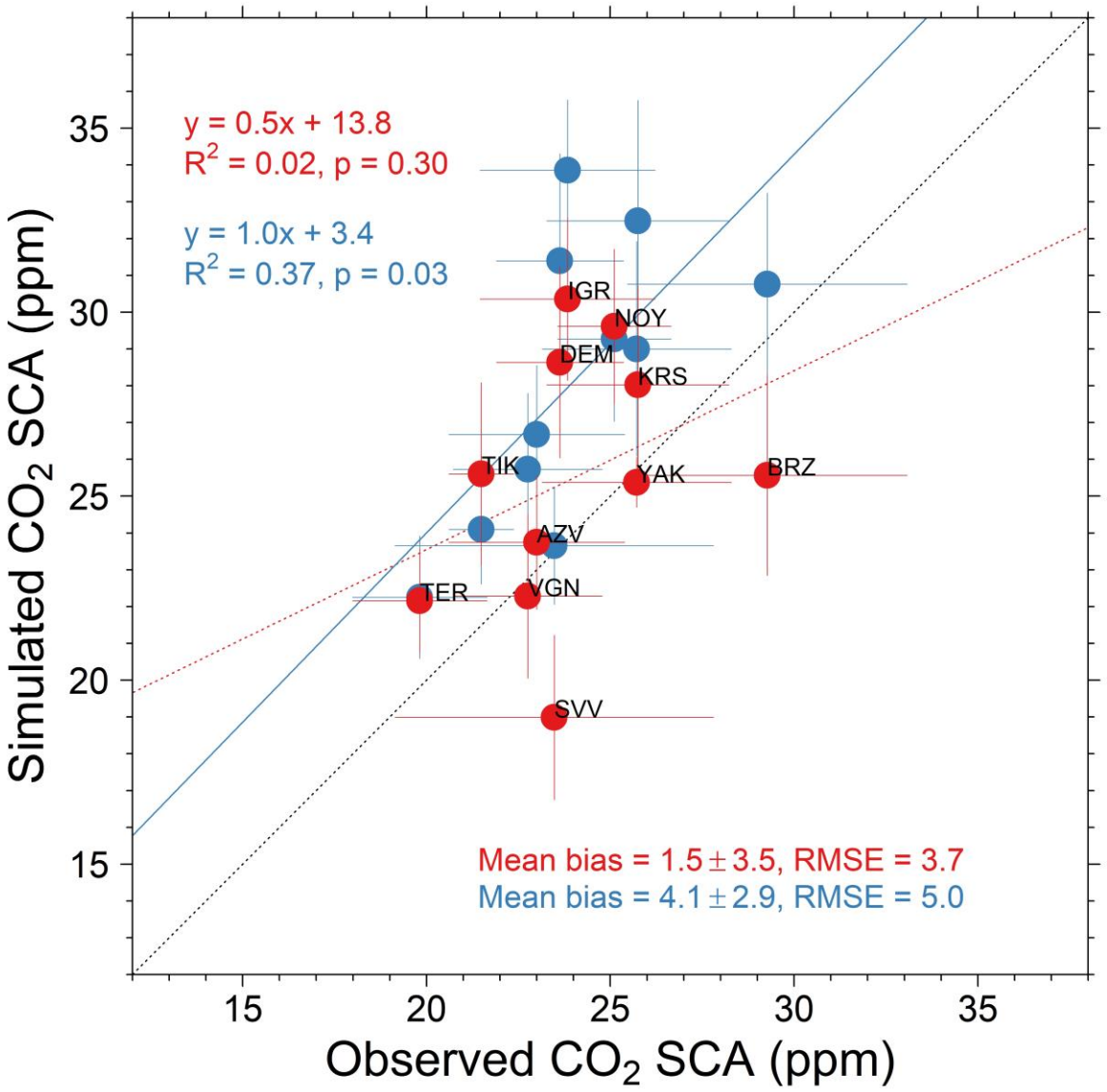

Figure S9 Evaluation of simulated versus observed CO_2 SCA at Russian sites. The simulated SCA are derived from model results with CAMSv17r1 (red) or CT2017 (blue). Observations from these Russian sites were assimilated in CT2017 but not in CAMSv17r1. The black dotted line represents the unit line, whereas the colored lines indicate the least squares regression lines between simulated versus observed CO_2 SCA. Error bars denote ±1σ.

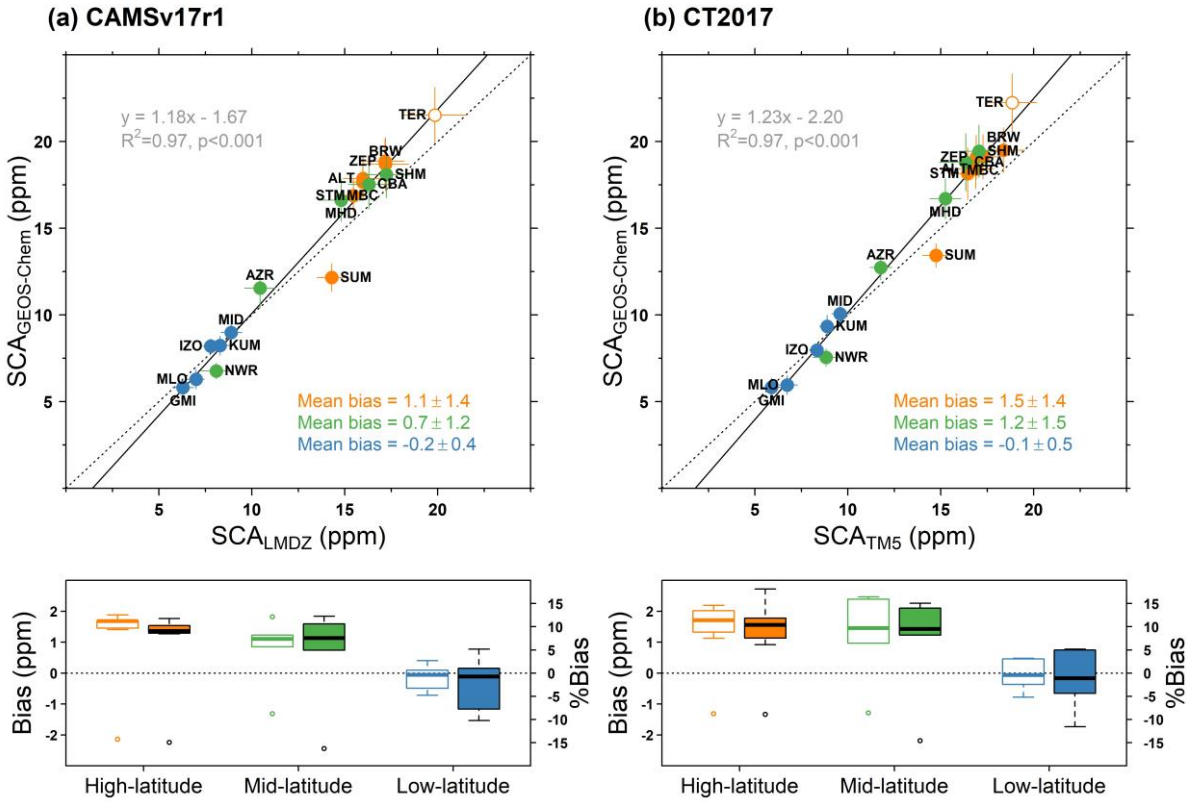

Figure S10 Comparison of CO_2 SCA simulated by GEOS-Chem versus **(a)** LMDz and **(b)** TM5. The SCA simulated by LMDz or TM5 at various stations were extracted from the posterior concentration fields of the CO_2 inversion CAMSv17r1 or CT2017. For each group of the boxplot, the box on the left (with the y axis on the left side) shows statistics of the model-observation bias, whereas the box on the right (with the y axis on the right side) shows the relative bias with respect to the SCA simulated by LMDz or TM5. The orange, green and blue circles, bars and texts indicate data and results for high-latitude (60–90°N), mid-latitude (30–60°N), and low-latitude (0–30°N) stations, respectively. Only the 16 stations from NOAA's GGGRN and the non-assimilated station Teriberka in Russia were included. Dotted and solid lines represent the unit line and least squares regression line, respectively. Error bars denote ±1σ.

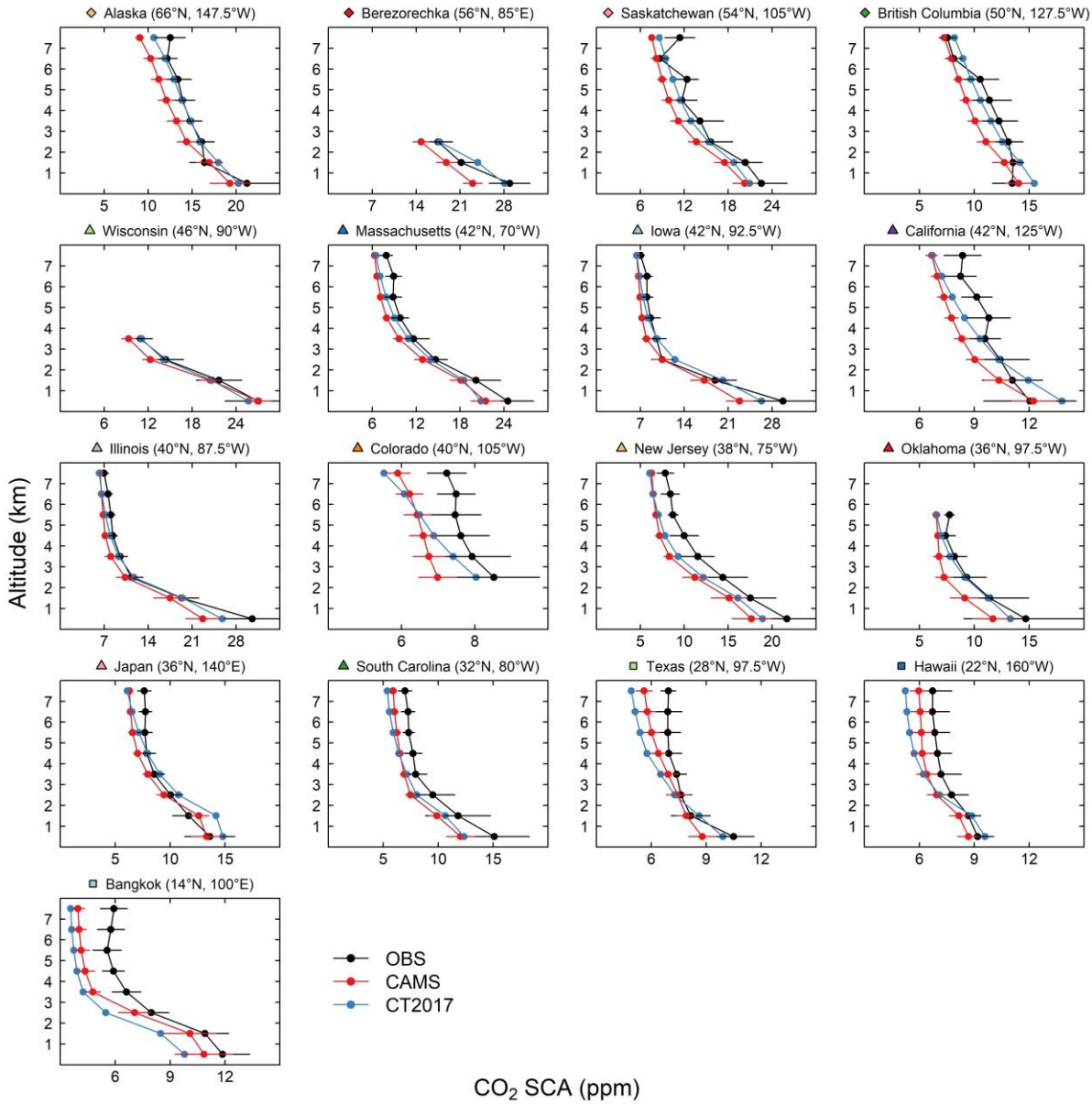

Figure S11 Simulated versus observed vertical profiles of CO_2 SCA at 17 aircraft sites. For each panel, black dots indicate CO_2 SCA from observations, while red and blue dots indicate simulated SCA from CO_2 inversion products CAMSv17r1 and CT2017, respectively. Both observed and simulated mean SCA were estimated over the time period when observations are available. Panels are arranged by latitudes and correspond to aircraft sites noted in **Fig. 1*A***. Error bars denote ±1σ.

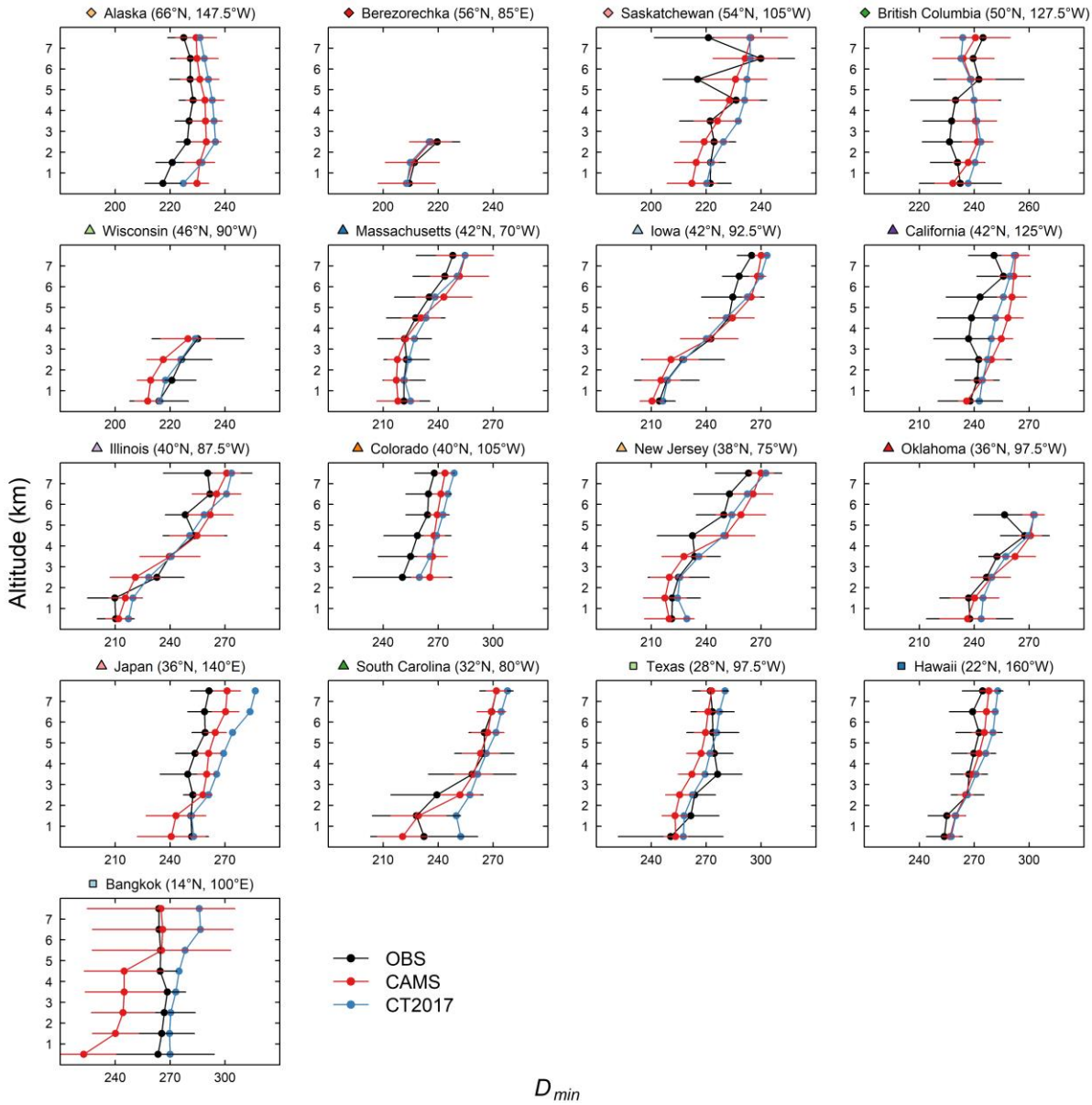

Figure S12 Simulated versus observed vertical profiles of the Julian day for CO_2 seasonal cycle minimum (D_{min}) at 17 aircraft sites. For each panel, black dots indicate D_{min} from observations, while red and blue dots indicate simulated D_{min} from CO_2 inversion products CAMSv17r1 and CT2017, respectively. Both observed and simulated D_{min} were estimated over the time period when observations are available. Panels are arranged by latitudes and correspond to aircraft sites noted in **Fig. 1*A***. Error bars denote ±1σ.

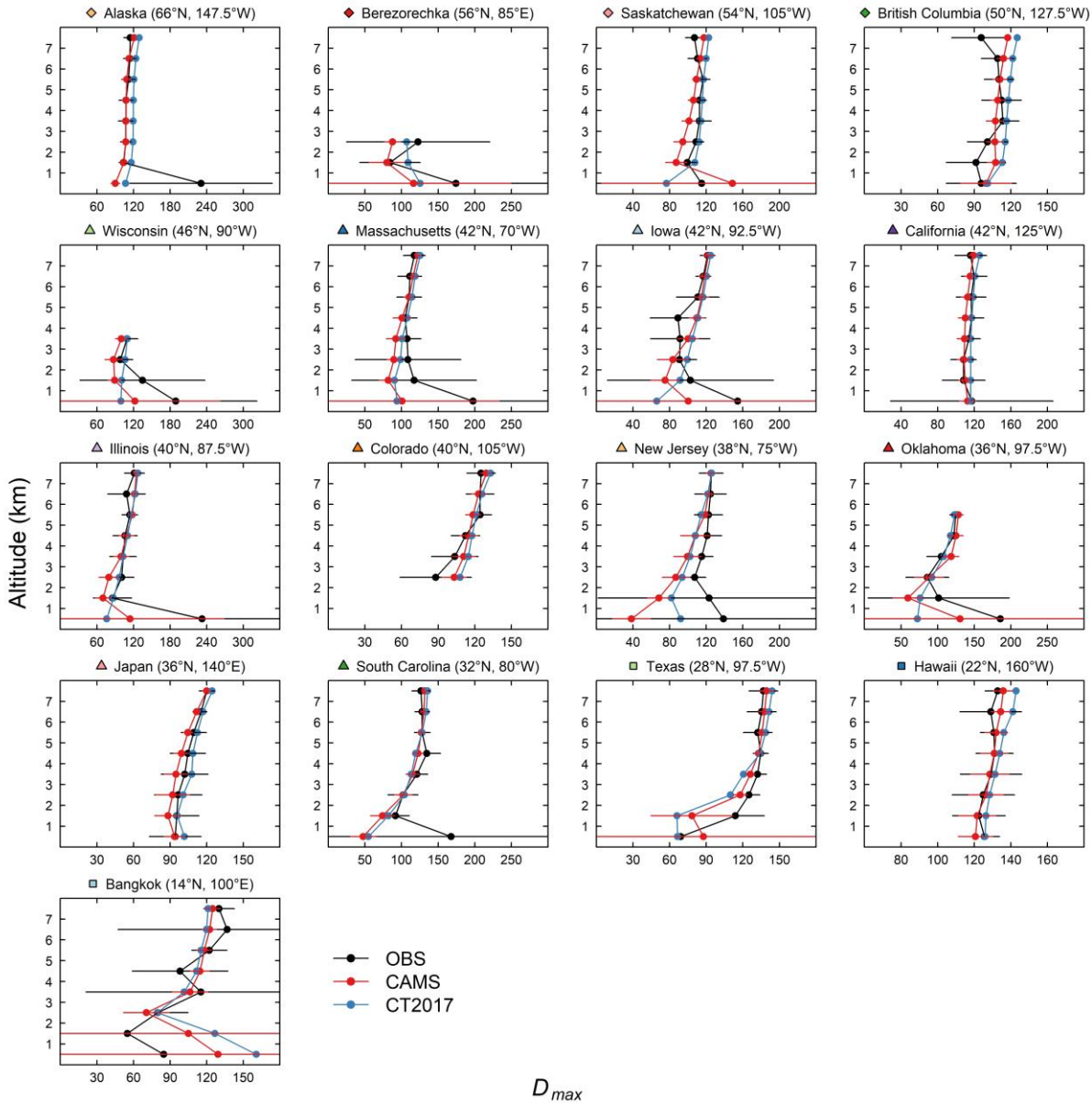

Figure S13 Simulated versus observed vertical profiles of the Julian day for CO_2 seasonal cycle maximum (D_{max}) at 17 aircraft sites. For each panel, black dots indicate D_{max} from observations, while red and blue dots indicate simulated D_{max} from CO_2 inversion products CAMSv17r1 and CT2017, respectively. Both observed and simulated D_{max} were estimated over the time period when observations are available. Panels are arranged by latitudes and correspond to aircraft sites noted in **Fig. 1*A***. Error bars denote ±1σ.

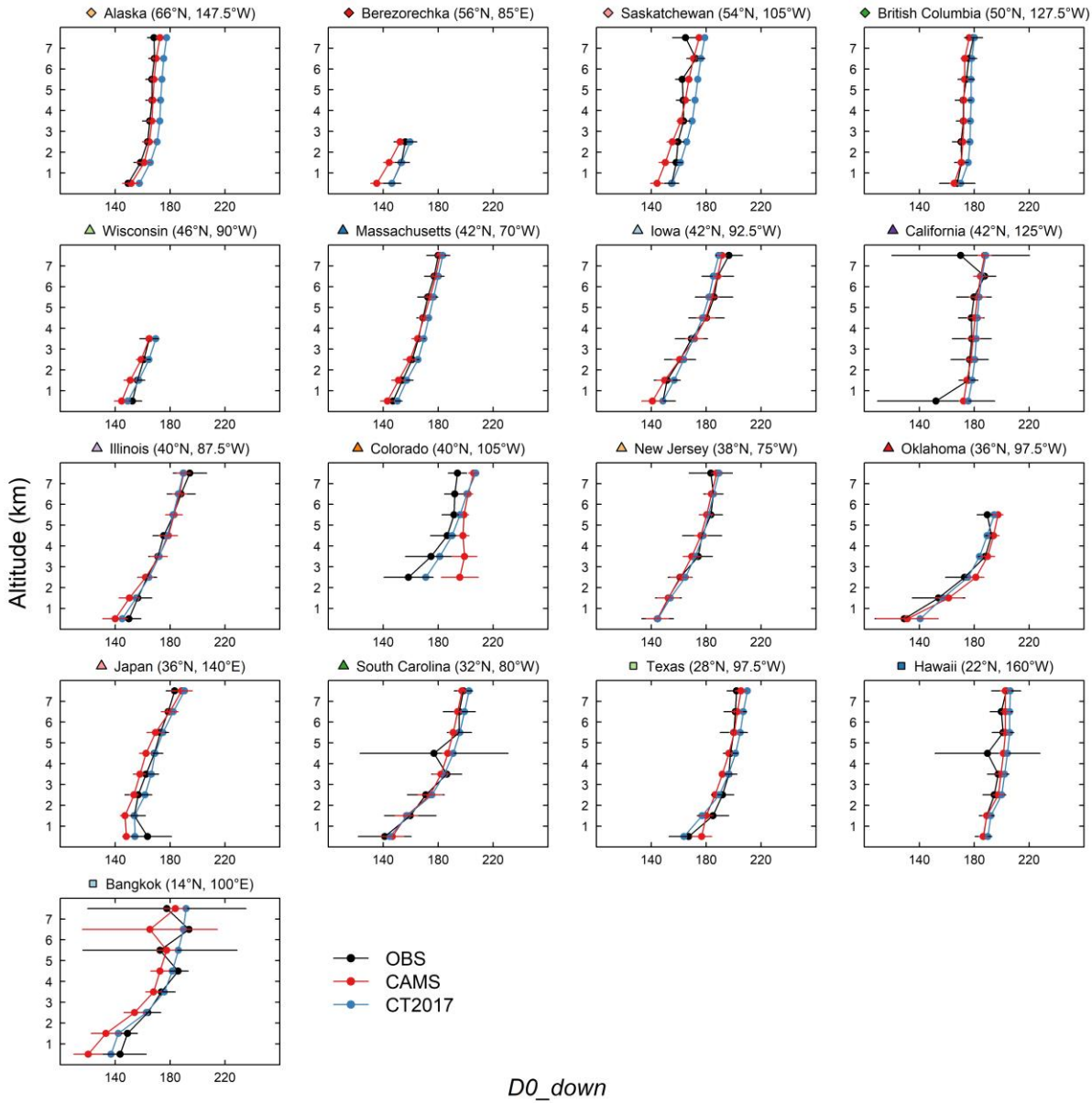

Figure S14 Simulated versus observed vertical profiles of the downward zero-crossing day for CO_2 seasonal cycle (*D0_down*) at 17 aircraft sites. For each panel, black dots indicate *D0_down* from observations, while red and blue dots indicate simulated *D0_down* from CO_2 inversion products CAMSv17r1 and CT2017, respectively. Both observed and simulated *D0_down* were estimated over the time period when observations are available. Panels are arranged by latitudes and correspond to aircraft sites noted in **Fig. 1*A***. Error bars denote ±1σ.

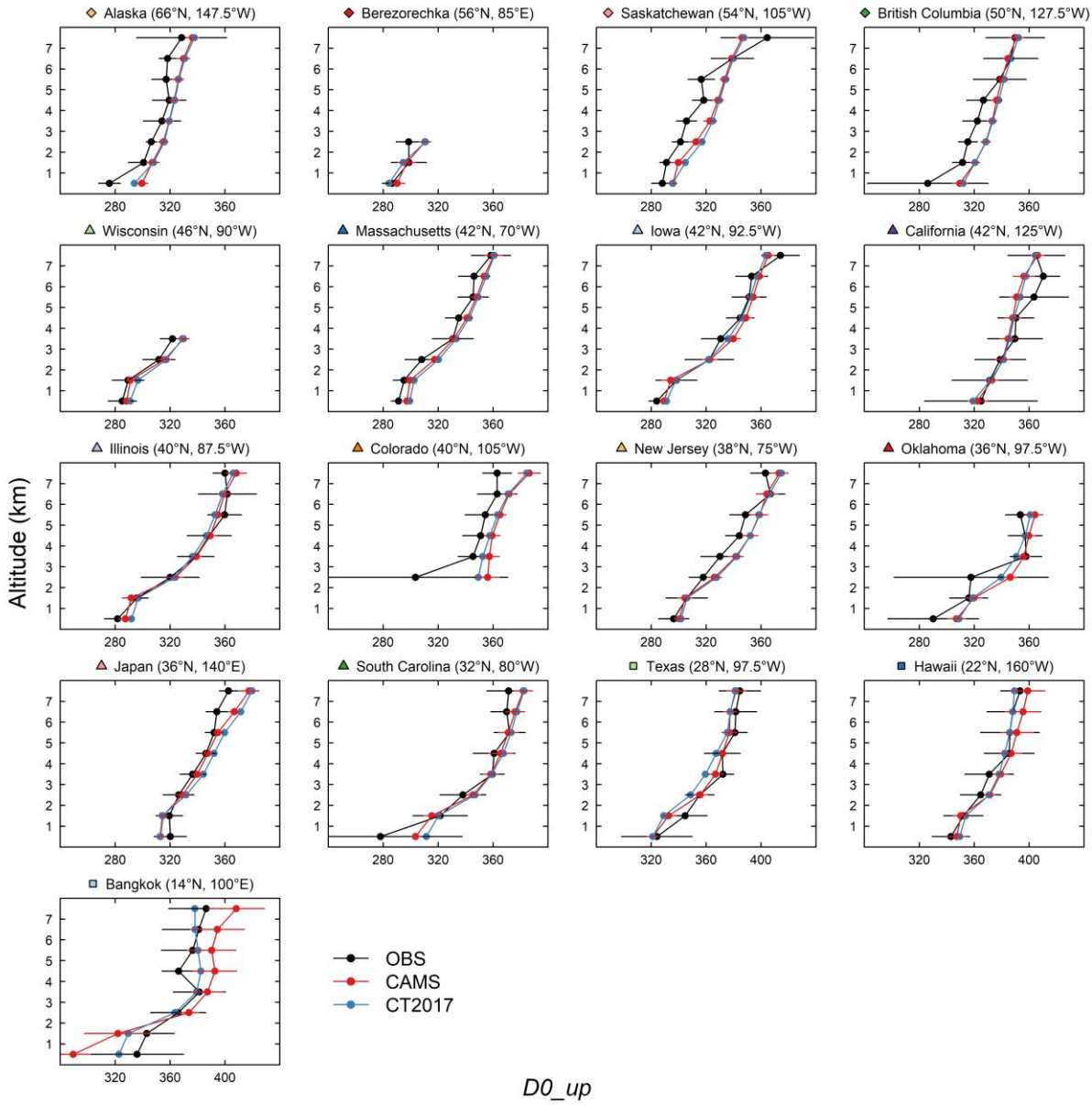

Figure S15 Simulated versus observed vertical profiles of the upward zero-crossing day for CO_2 seasonal cycle (*D0_up*) at 17 aircraft sites. For each panel, black dots indicate *D0_up* from observations, while red and blue dots indicate simulated *D0_up* from CO_2 inversion products CAMSv17r1 and CT2017, respectively. Both observed and simulated *D0_up* were estimated over the time period when observations are available. Panels are arranged by latitudes and correspond to aircraft sites noted in **Fig. 1*A***. Error bars denote ±1σ.

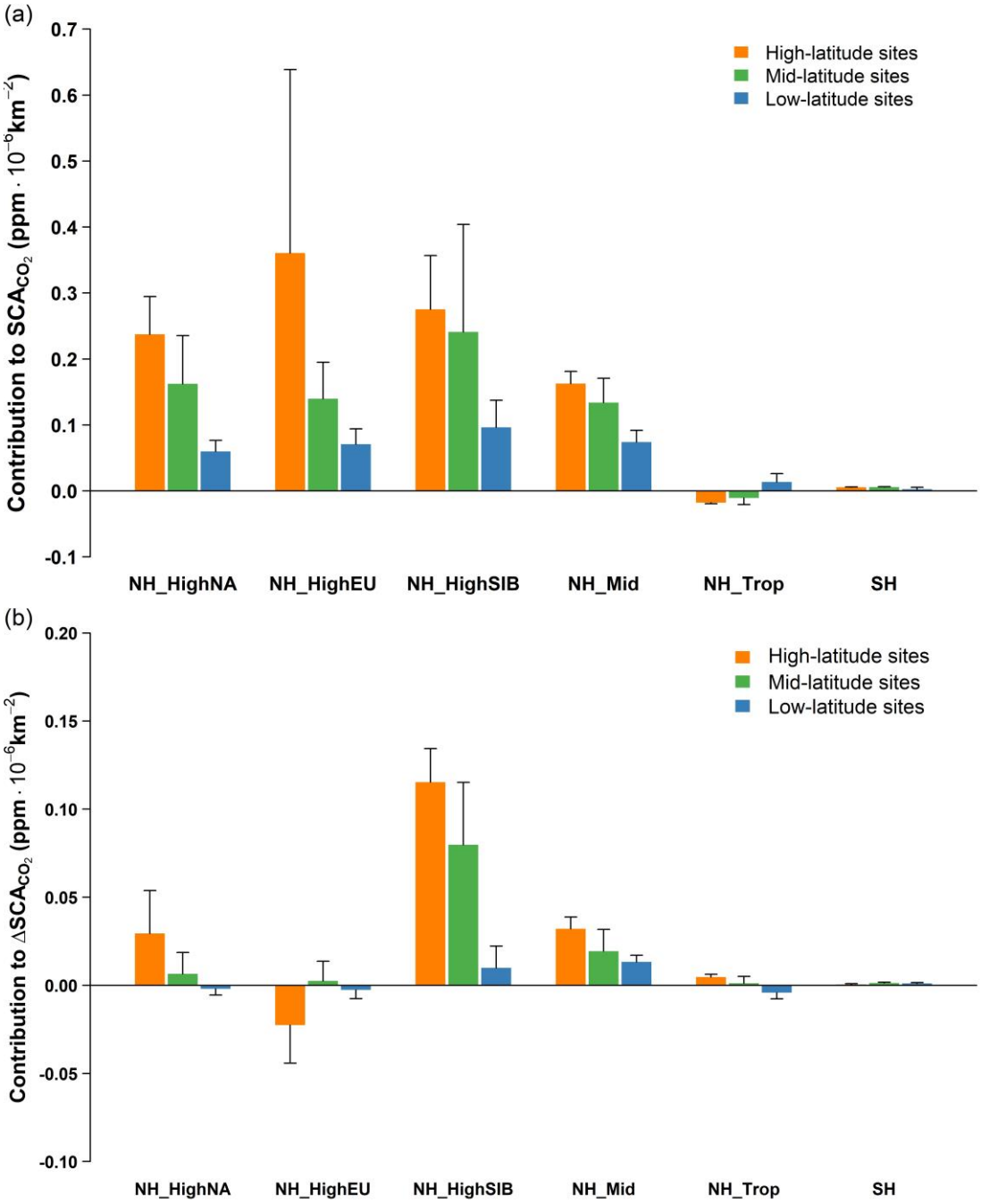

Figure S16 Contribution of the six major tagged regions to site-level **(a)** CO_2 SCA and **(b)** ΔSCA normalized by region size (in ppm·10^{-6}km^{-2}), based on simulations using the inverted fluxes from CAMSv17r1 for 1980–2017. The orange, green and blue bars represent flux imprints from different tagged regions on x-axis for northern high-latitude (60–90°N; n=7), mid-latitude (30–60°N; n=5) and low-latitude (0–30°N; n=5) stations, respectively. Only the 16 stations from NOAA's GGGRN and the non-assimilated station Teriberka in Russia were included.

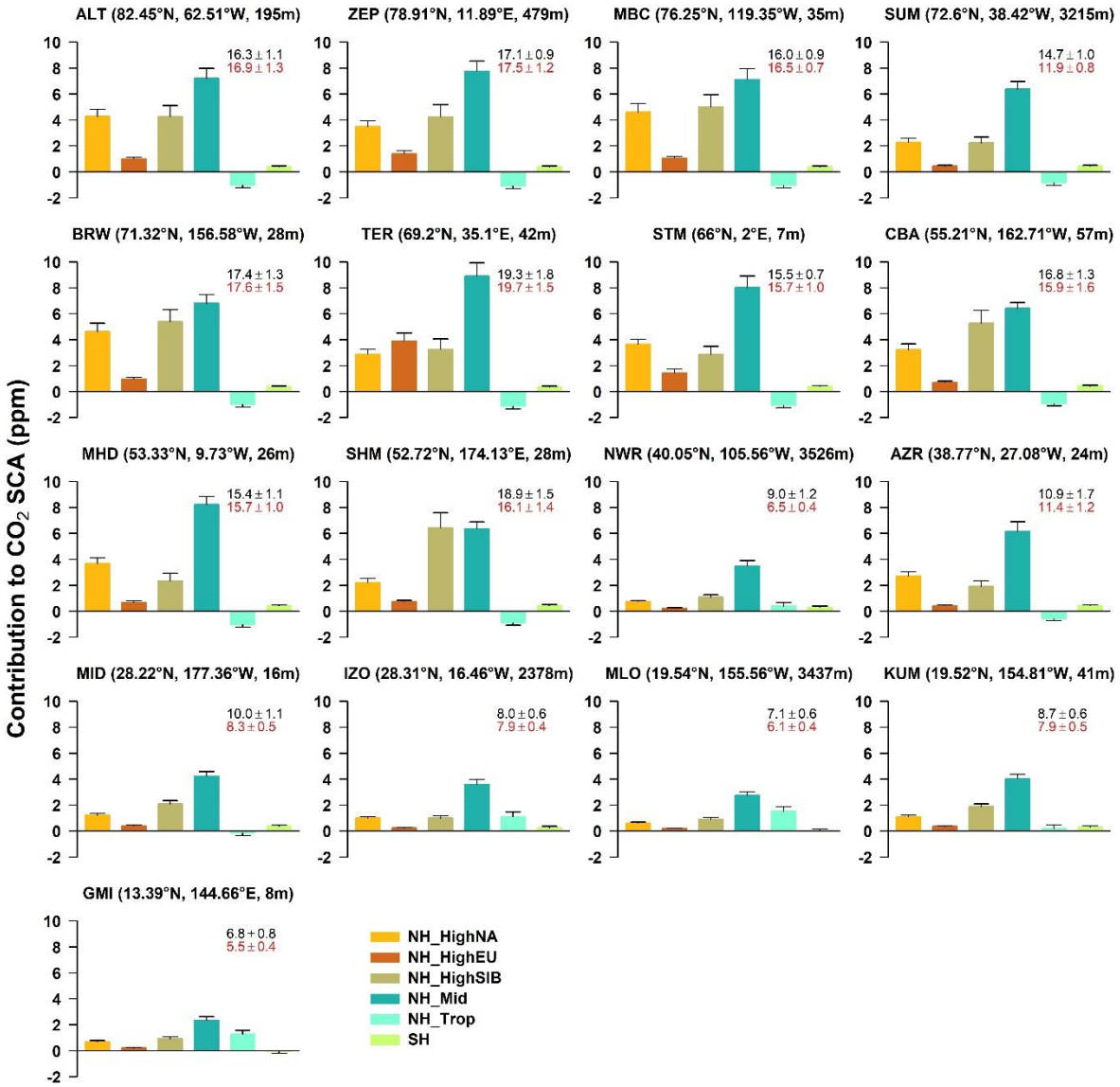

Figure S17 Contribution of different regions to CO_2 seasonal cycle amplitudes (SCA, in ppm) for 17 stations in the Northern Hemisphere, based on simulated CO_2 and tracer concentrations from CAMSv17r1 during 1980–2017. For each panel, the numbers on the top right indicate the observed (black) and simulated (red) mean SCA over the time period when observations are available. Panels are arranged by latitudes.

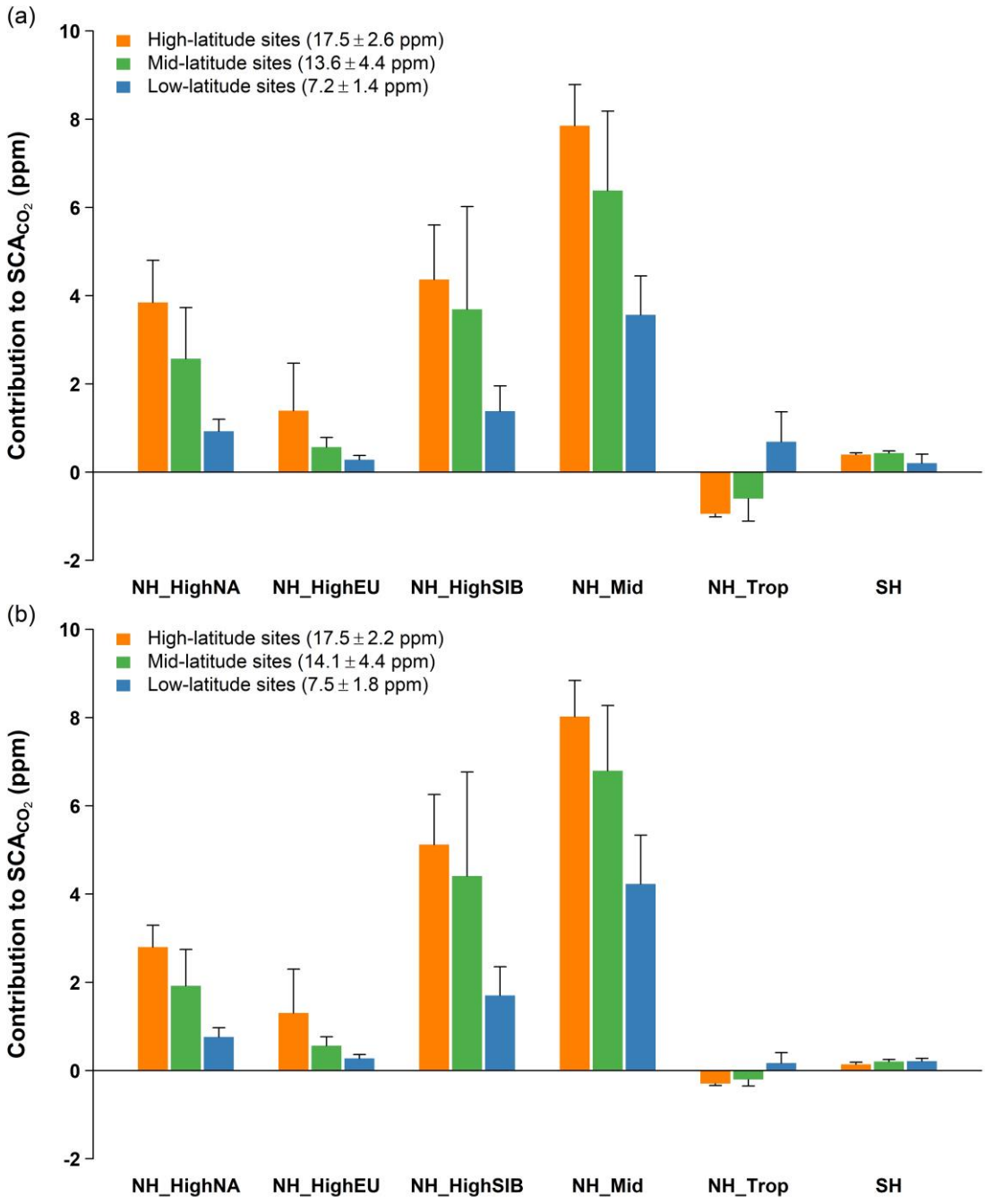

Figure S18 Contribution of the six major tagged regions to site-level CO_2 SCA, based on simulations using the inverted fluxes from **(a)** CAMSv17r1 and **(b)** CT2017 for 2000–2016. The orange, green and blue bars represent flux imprints from different tagged regions on x-axis for northern high-latitude (60–90°N; n=7), mid-latitude (30–60°N; n=5) and low-latitude (0–30°N; n=5) stations, respectively, with the numbers in the parentheses showing the mean SCA averaged within station groups. Only the 16 stations from NOAA's GGGRN and the non-assimilated station Teriberka in Russia are included.

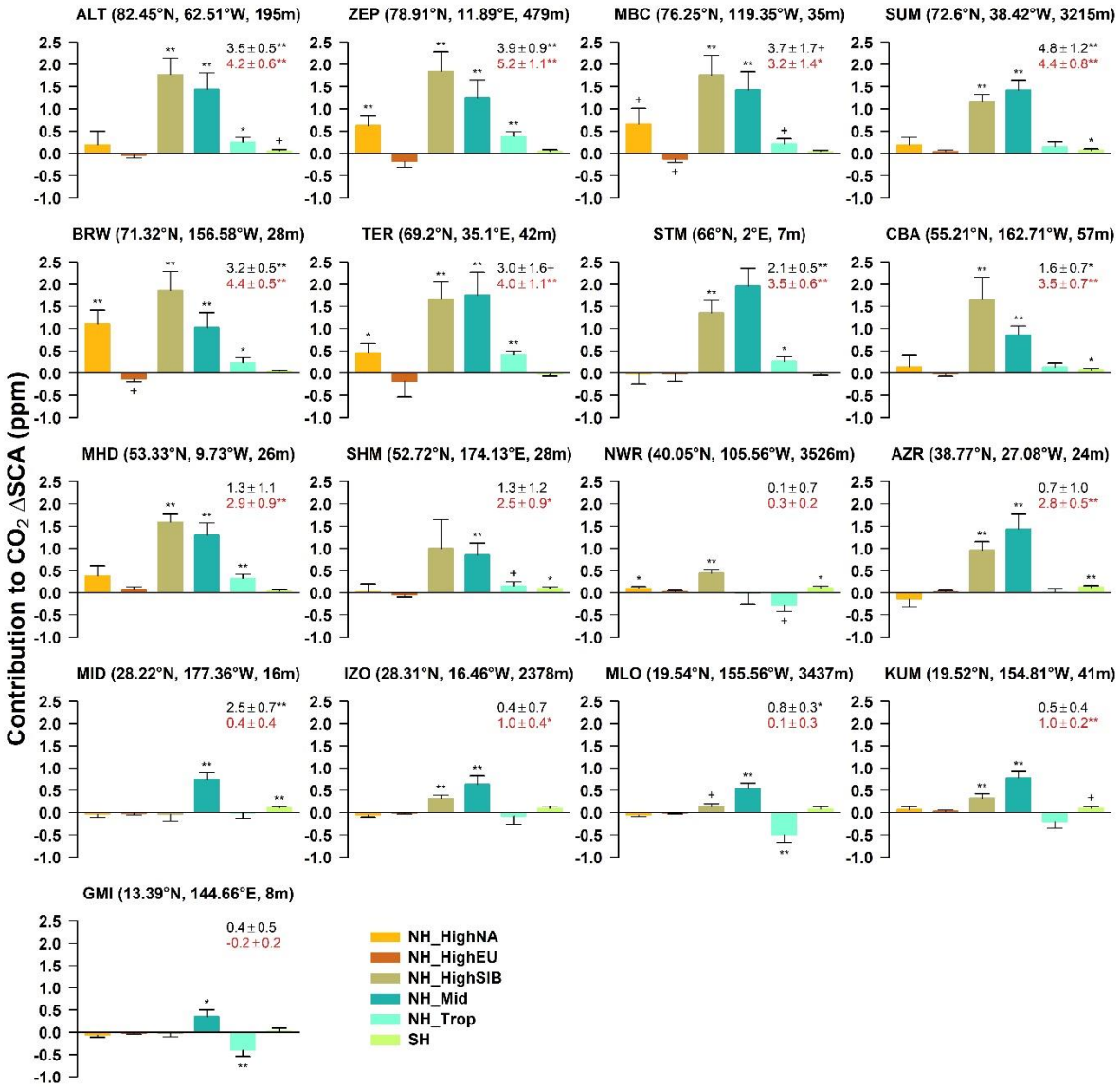

Figure S19 Contribution of different regions to changes in CO_2 seasonal cycle amplitudes (ΔSCA, in ppm) for 17 stations in the Northern Hemisphere, based on simulated CO_2 and tracer concentrations from CAMSv17r1 during 1980–2017. For each panel, the numbers on the top right indicate the observed (black) and simulated (red) mean ΔSCA over the time period when observations are available. Significance of trends is notated for CO_2 and respective tracers (** $p < 0.01$, * $p < 0.05$, $^{+}$ $p < 0.10$). Panels are arranged by latitudes.

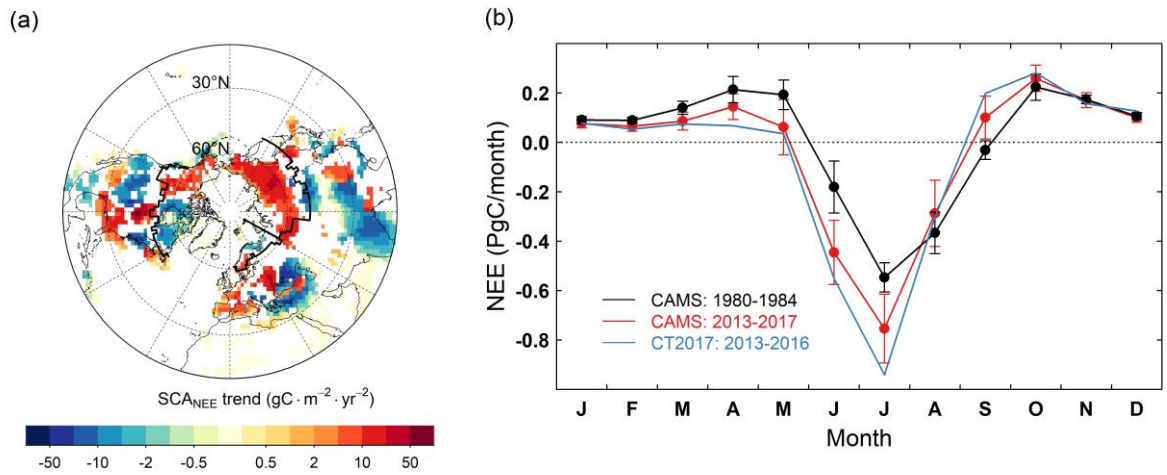

Figure S20 Trend in NEE seasonality for 1980–2017, based on fluxes from CAMSv17r1. **(a)** presents the spatial pattern of trend in the NEE seasonal amplitude (SCA_{NEE}). Only pixels with significant trends ($p < 0.05$) are shaded. The bold black lines delineate the three high-latitude tagged regions, i.e., NH_HighNA, NH_HighEU and NH_HighSIB. **(b)** presents a comparison of seasonal carbon exchanges between 2013–2017 and 1980–1984 averaged over Siberian ecosystems (i.e. the tagged region NH_HighSIB). The error bars for monthly fluxes are ±1σ posterior error standard deviation using the Monte Carlo method described in Ref. 12. The seasonal carbon exchange based on fluxes from CT2017 during 2013–2016 is also presented for comparison.

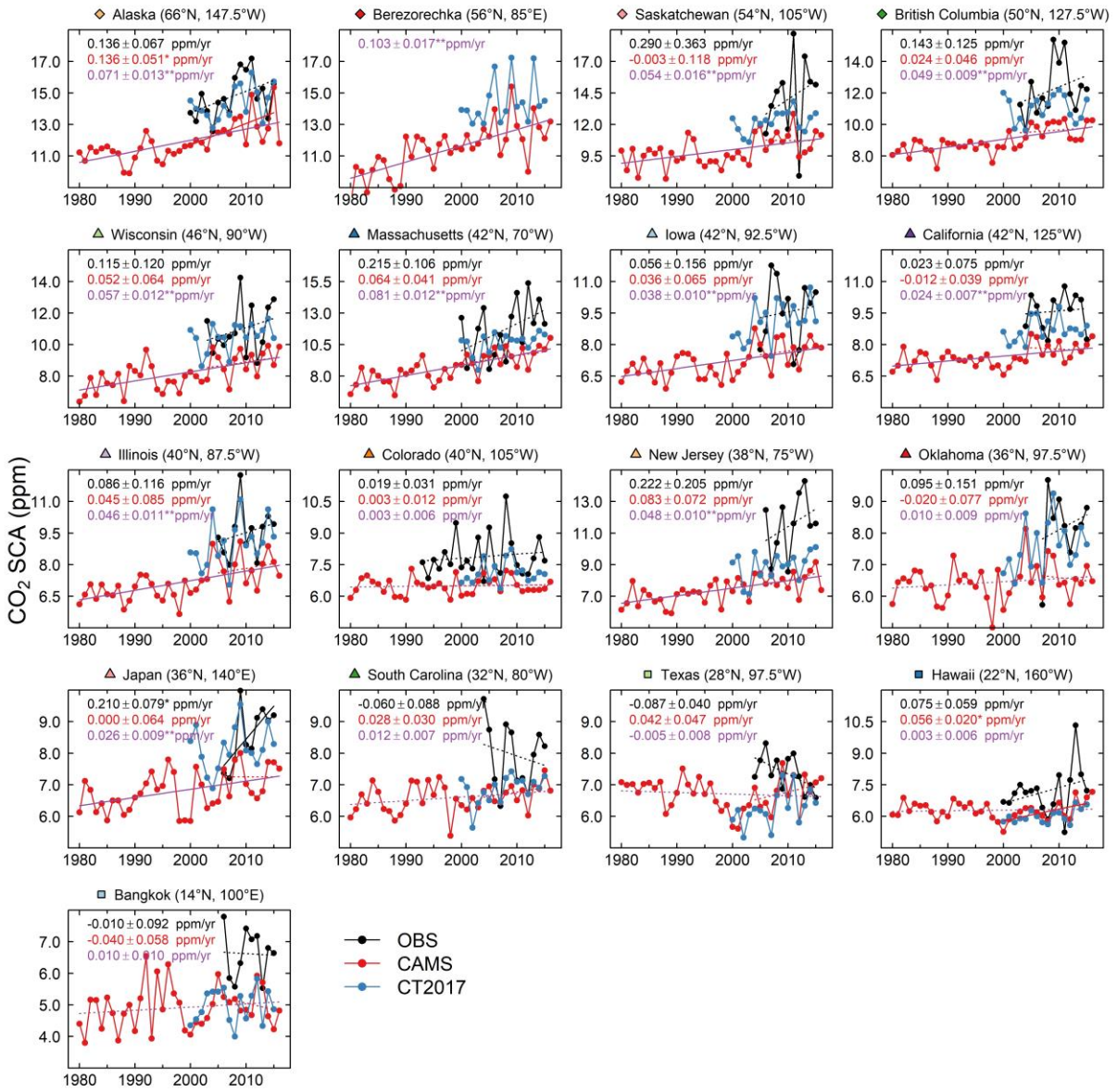

Figure S21 Time series of simulated and observed CO_2 SCA at the altitude 3–4 km for the 17 pixels selected for vertical profile evaluation. For each panel, black dots indicate CO_2 SCA from observations, while red and blue dots indicate simulated SCA from CO_2 inversion products CAMSv17r1 and CT2017, respectively. Both observed and simulated SCA from CAMSv17r1 were fitted over the time period when observations are available, show in black and red lines respectively, with trends given as well (** $p < 0.01$, * $p < 0.05$). Solid and dotted lines indicate significant and non-significant trends, respectively. For simulated SCA from CAMSv17r1, the fitted line and trend over the whole simulation period 1980–2017 are also shown in purple. Panels are arranged by latitudes and correspond to the aircraft sites noted in **Fig. 1*A***.

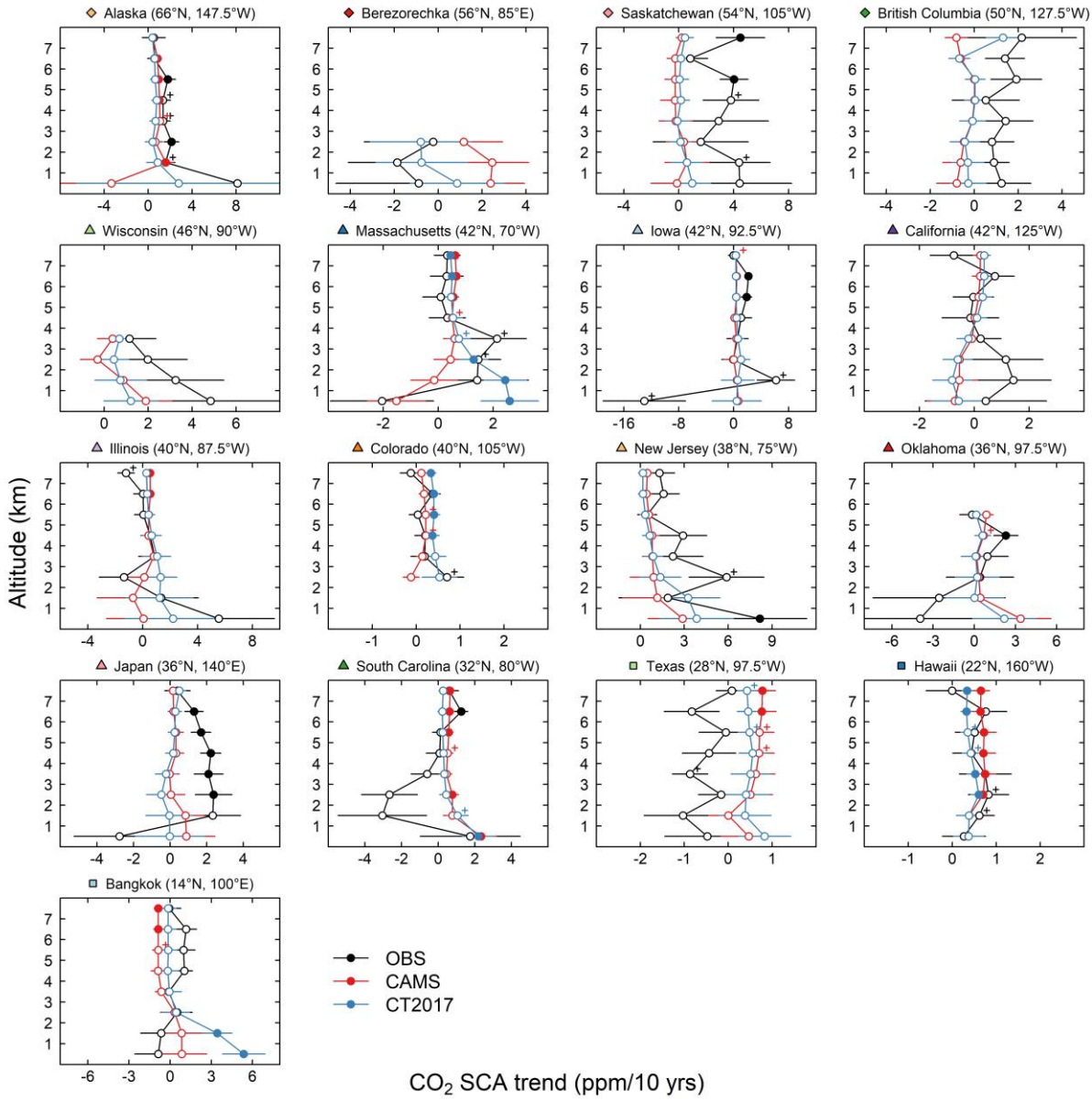

Figure S22 Evaluation of simulated versus observed vertical profiles of CO_2 SCA trends at 17 aircraft sites. For each panel, black dots indicate SCA trends from observations, while red and blue dots indicate simulated SCA trends from CO_2 inversion products CAMSv17r1 and CT2017, respectively. Both observed and simulated SCA trends are estimated over the time period when observations are available. Filled circles represent significant trends ($p < 0.05$), whereas open circles with "+" represent marginally significant trends ($p < 0.1$). Panels are arranged by latitudes and correspond to the aircraft sites noted in **Fig. 1*A***. Error bars denote ±1σ.

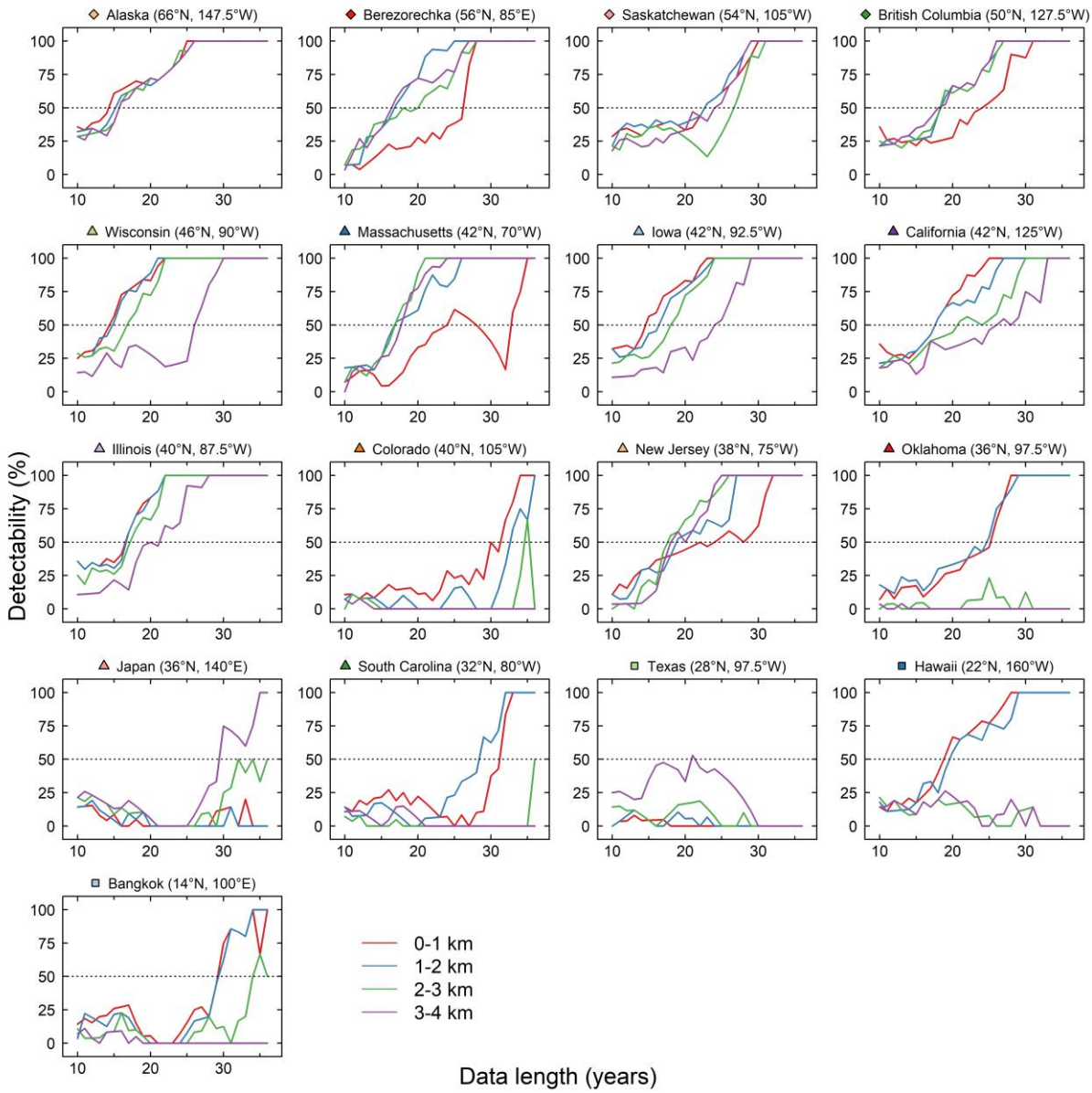

Figure S23 Significance of the SCA trend as a function of data record length based on model results at 17 aircraft sites. For the definition of detectability of significant trend, see *Materials and Methods* for details. The point of intersection between each curve and the horizontal dotted line represents the minimal data length required to achieve ≥50% detectability of significant trend. Panels are arranged by latitudes and correspond to the aircraft sites noted in **Fig. 1*A***.

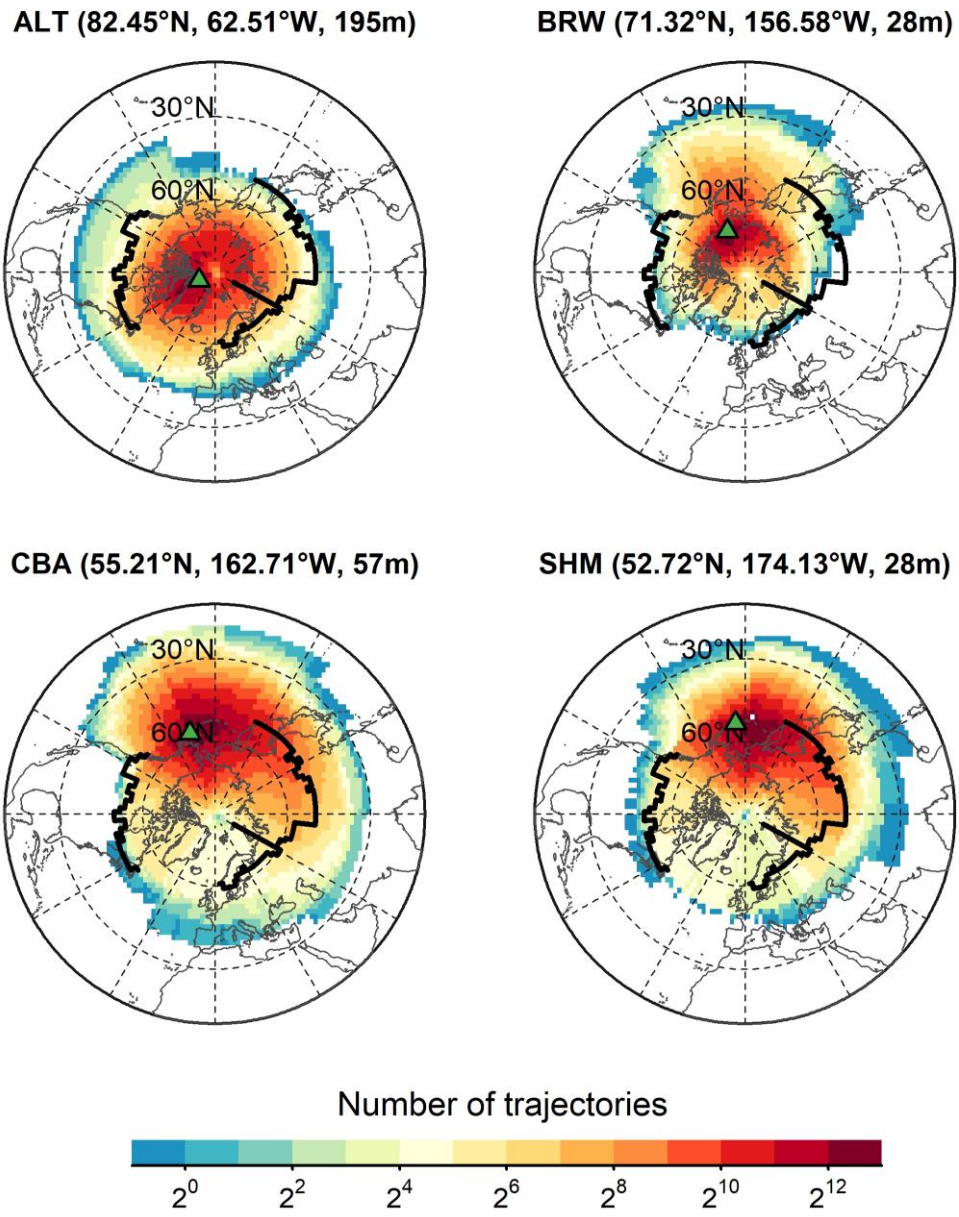

Figure S24 Footprint maps showing origins of air masses for Alert (ALT), Utqiagvik (Barrow, BRW), Cold Bay (CBA) and Shemya Island (SHM). For each station, individual 168-hour backward trajectories were reconstructed for the year 2015 at an hourly frequency, using the HYbrid Single-Particle Lagrangian Integrated Trajectory (HYSPLIT) model (13–15) driven by the 3-hourly meteorological fields from the Global Data Assimilation System (GDAS) archive run by National Centers for Environmental Prediction (NECP). Maps are color-coded based on the number of trajectories passing through each grid cell. The bold black lines delineate the three high-latitude tagged regions, i.e., NH_HighNA, NH_HighEU and NH_HighSIB.

References

1. Landschützer P, et al. (2015) The reinvigoration of the Southern Ocean carbon sink. *Science* 349(6253):1221–4.

2. Takahashi T, et al. (2009) Climatological mean and decadal change in surface ocean pCO_2, and net sea–air CO_2 flux over the global oceans. *Deep Sea Res Part II Top Stud Oceanogr* 56(8–10):554–577.

3. Chevallier F, et al. (2010) CO_2 surface fluxes at grid point scale estimated from a global 21 year reanalysis of atmospheric measurements. *J Geophys Res* 115(D21):D21307.

4. Chevallier F, et al. (2005) Inferring CO_2 sources and sinks from satellite observations: Method and application to TOVS data. *J Geophys Res* 110(D24):D24309.

5. Peters W, et al. (2007) An atmospheric perspective on North American carbon dioxide exchange: CarbonTracker. *Proc Natl Acad Sci U S A* 104(48):18925–30.

6. Dlugokencky EJ, et al. (2018) *Atmospheric Carbon Doixide Dry Air Mole Fractions from the NOAA ESRL Carbon Cycle Cooperative Global Air Sampling Network, 1968-2017, Version: 2018-07-31* Available at: ftp://aftp.cmdl.noaa.gov/data/trace_gases/co2/flask/surface/.

7. Sasakawa M, et al. (2013) Aircraft and tower measurements of CO_2 concentration in the planetary boundary layer and the lower free troposphere over southern taiga in West Siberia: Long-term records from 2002 to 2011. *J Geophys Res Atmos* 118(16):9489–9498.

8. Sasakawa M, et al. (2010) Continuous measurements of methane from a tower network over Siberia. *Tellus B Chem Phys Meteorol* 62(5):403–416.

9. Sweeney C, et al. (2018) *NOAA Carbon Cycle and Greenhouse Gases Group aircraft-based measurements of CO_2, CH_4, CO, N_2O, H_2 and SF_6 in flask-air samples taken since 1992* (NOAA Earth System Research Laboratory, Global Monitoring Division) Available at: http://dx.doi.org/10.7289/V5N58JMF.

10. Machida T, Matsueda H, Sawa Y, Niwa Y (2018) Atmospheric CO_2 mole fraction data of CONTRAIL-CME. doi:10.17595/20180208.001.

11. Machida T, et al. (2008) Worldwide Measurements of Atmospheric CO_2 and Other Trace Gas Species Using Commercial Airlines. *J Atmos Ocean Technol* 25(10):1744–1754.

12. Chevallier F, Bréon F-M, Rayner PJ (2007) Contribution of the Orbiting Carbon Observatory to the estimation of CO_2 sources and sinks: Theoretical study in a variational data assimilation framework. *J Geophys Res* 112(D9):D09307.

13. Draxler RR, Hess GD (1998) An overview of the HYSPLIT_4 modeling system of trajectories, dispersion, and deposition. *Aust Meteor Mag* 47:295–308.

14. Draxler RR (1999) *HYSPLIT4 user's guide. NOAA Tech. Memo. ERL ARL-230* (Silver Spring, MD).

15. Stein AF, et al. (2015) NOAA's HYSPLIT atmospheric transport and dispersion modeling system. *Bull Am Meteorol Soc* 96(12):2059–2077.